

Search for Neutral Triple Gauge Couplings with ZZ Production at Future Electron Positron Colliders

Yu-Chen Guo^{a,b} Chun-Jing Pan^a Man-Qi Ruan^{c,d} Ji-Chong Yang,^{a,b,1}

^a*Department of Physics, Liaoning Normal University, No. 850 Huanghe Road, Dalian 116029, China*

^b*Center for Theoretical and Experimental High Energy Physics, Liaoning Normal University, No. 850 Huanghe Road, Dalian 116029, China*

^c*Institute of High Energy Physics, Chinese Academy of Sciences, 19B Yuquan Road, Shijingshan District, Beijing 100049, China*

^d*University of Chinese Academy of Sciences, 19A Yuquan Road, Shijingshan District, Beijing 100049, China*

E-mail: ycguo@lnnu.edu.cn, panchunjing2022@163.com, ruanmq@ihep.ac.cn, yangjichong@lnnu.edu.cn

ABSTRACT: This study investigates Neutral Triple Gauge Couplings (nTGCs) through ZZ production at future electron-positron colliders. The impact of beam polarization on cross section is analyzed. We compare the signals and backgrounds for five different ZZ decay channels and present our event selection strategies for future e^+e^- colliders. The expected coefficient constraints for each decay channels are provided, and final expected constraints are derived by combining results from the different decay patterns. Our analysis indicates that future electron-positron colliders will have significantly enhanced detection capabilities for nTGCs compared to the current LHC experiments, with expected improvements in constraints by one to two orders of magnitude.

¹Corresponding author.

Contents

1	Introduction	1
2	ZZ production at e^+e^- colliders	3
3	Probing nTGCs via ZZ production at the future e^+e^- colliders	7
3.1	Selection of $e^+e^- \rightarrow 2\ell 2\ell'$	7
3.2	Selection of $e^+e^- \rightarrow 4j$	13
3.3	Selection of $e^+e^- \rightarrow 2\ell 2j$	16
3.4	Selection of $e^+e^- \rightarrow \ell^+\ell^-\nu\bar{\nu}$	20
3.5	Selection of $e^+e^- \rightarrow jj\nu\bar{\nu}$	24
3.6	Constraints on the coefficients with combined results	28
4	Conclusions	30
A	Helicity amplitudes	31

1 Introduction

In the absence of clear signals of new physics (NP) beyond the Standard Model (SM) from the Large Hadron Collider (LHC) experiments so far, the indirect detection of signs of new physics through precise measurements of SM processes has gained more attention. When the mass of a new particle is significantly larger than the electroweak symmetry breaking scale, the Standard Model Effective Field Theory (SMEFT) provides a systematic parameterization of NP effects [1–5], with the advantage of not relying on any particular model. The Lagrangian of SMEFT consists of operators of dimension-4, representing the SM itself, as well as higher-dimensional operators constructed from SM fields. The Lagrangian of SMEFT then takes the form

$$\mathcal{L}_{\text{SMEFT}} = \mathcal{L}_{\text{SM}} + \sum_{d=5}^{\infty} \sum_j \frac{C_j^{(d)}}{\Lambda^{d-4}} \mathcal{O}_j^{(d)},$$

where $\mathcal{O}^{(d)}$ is an operator of dimension d invariant under the $SU(3)_c \times SU(2)_L \times U(1)_Y$ gauge group of the SM, Λ represents the mass scale of new particles, with the power of Λ in each term determined by dimensional analysis, and $C_j^{(d)}$ is the Wilson coefficient of the operator. For any new physics model that satisfies the above assumptions, integrating out the new fields will produce a Lagrangian with this structure.

Depending on the gauge symmetry, triple gauge couplings (TGC) and quartic gauge couplings (QGC) exist in the SM. Measurements of these couplings not only test the nature of spontaneous electroweak symmetry breaking (EWSB) but also provide a unique window

for searching for new physics. Anomalous gauge couplings beyond the SM do not appear in the dimension-4 terms of the SM Lagrangian, and first arise in the dimension-6 terms of SMEFT. Neutral triple gauge coupling (nTGC) [6–9] and the gluonic quadratic gauge coupling (gQGC) [10] all arise first in gauge-invariant dimension-8 operators. Any sign of their detection would provide direct prima facie evidence for the existence of new physics. Additionally, it has been shown that dimension-8 operators play a crucial role from the convex geometry perspective within the SMEFT space [11]. Many researchers have emphasised the importance of dimension-8 operators [12–18].

In general, the contribution of dimension-6 operators to new physics is larger than that of dimension-8 or higher operators. Consequently, there are fewer experimental probes and constraint studies on dimension-8 SMEFT interactions. However, in some cases, dimension-8 operators can make leading contributions to NP processes. Examples include dimension-8 operators contributing to light-by-light scattering [19], vector boson scattering (VBS) [20–28], di-boson productions [29–37], and tri-boson productions [38–41]. Many experimental measurements have been made at the LHC [42–56].

At dimension-8, there are four CP-conserving operators contributing to nTGCs, they are [6, 8]

$$\begin{aligned} \mathcal{L}_{\text{nTGC}} = & \frac{\text{sign}(c_{\tilde{B}W})}{\Lambda_{\tilde{B}W}^4} \mathcal{O}_{\tilde{B}W} + \frac{\text{sign}(c_{B\tilde{W}})}{\Lambda_{B\tilde{W}}^4} \mathcal{O}_{B\tilde{W}} \\ & + \frac{\text{sign}(c_{\tilde{W}W})}{\Lambda_{\tilde{W}W}^4} \mathcal{O}_{\tilde{W}W} + \frac{\text{sign}(c_{\tilde{B}\tilde{B}})}{\Lambda_{\tilde{B}\tilde{B}}^4} \mathcal{O}_{\tilde{B}\tilde{B}}, \end{aligned} \quad (1.1)$$

with

$$\begin{aligned} \mathcal{O}_{\tilde{B}W} &= iH^+ \tilde{B}_{\mu\nu} W^{\mu\rho} \{D_\rho, D^\nu\} H + h.c., \\ \mathcal{O}_{B\tilde{W}} &= iH^+ B_{\mu\nu} \tilde{W}^{\mu\rho} \{D_\rho, D^\nu\} H + h.c., \\ \mathcal{O}_{\tilde{W}W} &= iH^+ \tilde{W}_{\mu\nu} W^{\mu\rho} \{D_\rho, D^\nu\} H + h.c., \\ \mathcal{O}_{\tilde{B}\tilde{B}} &= iH^+ \tilde{B}_{\mu\nu} B^{\mu\rho} \{D_\rho, D^\nu\} H + h.c., \end{aligned} \quad (1.2)$$

where $\tilde{B}_{\mu\nu} \equiv \epsilon_{\mu\nu\alpha\beta} B^{\alpha\beta}$, $\tilde{W}_{\mu\nu} \equiv \epsilon_{\mu\nu\alpha\beta} W^{\alpha\beta}$ and $W_{\mu\nu} \equiv W_{\mu\nu}^a \sigma^a / 2$ where σ^a are Pauli matrices. For simplicity, we define $f_X \equiv \text{sign}(c_X) / \Lambda_X^4$.

On the theoretical side, anomalous tensorial structures can be generated within a renormalizable theory at higher loop orders. For example, these structures can arise through a fermion triangle diagram in the Standard Model (SM). Loop-generated anomalous couplings have been studied in the Minimal Supersymmetric Standard Model (MSSM) [57–59] and the Little Higgs model [60]. A non-commutative extension of the SM (NCSM) [61, 62] can also provide an anomalous coupling structure in the neutral sector, with the possibility of a trilinear $\gamma\gamma\gamma$ coupling [61]. Additionally, the effective couplings ZZZ and $ZZ\gamma$ can be observed as deviations from the SM prediction in the measured Z -pair cross section, which have been proposed in the context of two-Higgs-doublet models [63, 64] and in low scale gravity theories [65].

Future e^+e^- colliders have great physics potential and provide one of the rare direct windows to NP at dimension-8. Previous studies have thoroughly studied probing nTGCs

by measuring $Z\gamma$ production at future e^+e^- colliders [31, 32, 35–37, 66–68] and pp colliders [33, 34, 69]. In this work, we study how nTGCs can be probed by measuring the $e^+e^- \rightarrow ZZ$ process with decays at different versions of circular and linear e^+e^- colliders, including the CEPC [70], ILC [71], and CLIC [72].

The plan of this paper is as follows. In Section 2, we discuss the beam polarization effects on cross section of ZZ production at e^+e^- colliders. In Section 3, we compare the signals and backgrounds of five ZZ decay channels and present our event selection strategy for e^+e^- colliders with different energies and luminosities. The expected constraints on the coefficients with combined results are also presented in Section 3. Finally, we summarize our conclusions in Section 4. We compare the results obtained with experimental measurements of nTGCs from the LHC [73]. Depending on the capabilities of different future lepton colliders to detect nTGCs, their sensitivity could exceed that of the current LHC. The $e^+e^- \rightarrow ZZ$ process will thus provide a unique and promising channel for the detection of new physics at future lepton colliders.

2 ZZ production at e^+e^- colliders

At future electron-positron colliders, the di-boson pair production can be an interesting topic and ideal motivation. In this Section, we first discuss the cross section of the $e^+e^- \rightarrow ZZ$ process induced by nTGCs and the contribution of the Standard Model to this process. We then analyze the influence of initial electron polarization on the cross section.

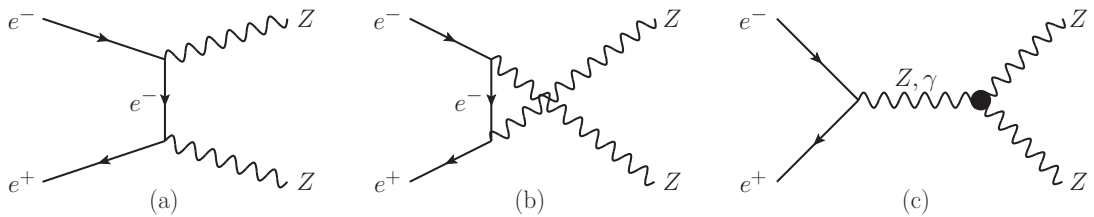


Figure 1: Feynman diagrams of the $e^+e^- \rightarrow ZZ$ production. Diagrams (a) and (b) are the SM contributions. Diagram (c) corresponds to contributions from the nTGCs.

In the SM, the process $e^+e^- \rightarrow ZZ$ proceeds via the t - and u -channel exchange diagrams at tree level. The presence of nTGCs would lead to a sizable enhancement of ZZ final states via s -channel e^+e^- scattering. The Feynman diagrams are shown in Fig. 1.

The process of $e^+e^- \rightarrow ZZ$ can be affected by dimension-8 operators through the ZZZ and $ZZ\gamma$ couplings. In the case of ZZV coupling with the Z boson and γ on-shell, there is only one independent operator because the $\mathcal{O}_{B\tilde{W}}$ operator is equivalent to the $\mathcal{O}_{\tilde{B}W}$ operator, and the $\mathcal{O}_{\tilde{W}W}$ and $\mathcal{O}_{\tilde{B}B}$ operators do not contribute [8]. We focus on the $\mathcal{O}_{\tilde{B}W}$ operator for this nTGC study. At the leading order of s , the analytical cross sections are given by

$$\begin{aligned}
\sigma_{\text{nTGC}}(ZZ) &= \frac{f_{\tilde{B}W}^2 c_W^2 M_Z^2 s_W^2 (s - 4M_Z^2)^{\frac{5}{2}}}{24\pi\sqrt{s}}, \\
\sigma_{\text{int}}(ZZ) &= \frac{f_{\tilde{B}W} e^2 M_Z^2 (4s_W^2 - 1) \sqrt{s - 4M_Z^2}}{32\pi c_W s^{\frac{3}{2}} s_W \sqrt{s(s - 4M_Z^2)}} \\
&\quad \times \left[(2M_Z^2 + s) \sqrt{s(s - 4M_Z^2)} - 4M_Z^2 (s - M_Z^2) \tanh^{-1} \left(\frac{\sqrt{s(s - 4M_Z^2)}}{s - 2M_Z^2} \right) \right], \quad (2.1) \\
\sigma_{\text{SM}}(ZZ) &= \frac{e^4 \sqrt{s - 4M_Z^2} (32c_W^8 - 96c_W^6 + 120c_W^4 - 72c_W^2 + 17)}{128\pi c_W^4 s^2 s_W^4 (2M_Z^2 - s) \sqrt{s - 4M_Z^2}} \\
&\quad \times \left[\sqrt{s(s - 2M_Z^2)} \sqrt{s - 4M_Z^2} - (4M_Z^4 + s^2) \tanh^{-1} \left(\frac{\sqrt{s}\sqrt{s - 4M_Z^2}}{s - 2M_Z^2} \right) \right].
\end{aligned}$$

The anomalous ZZZ and $ZZ\gamma$ couplings are allowed by electromagnetic gauge invariance and Lorentz invariance for on-shell Z and γ bosons. The $ZZ\gamma$ coupling is absent at tree level and is highly suppressed when allowed by internal particle loops in the SM, thus forbidding the s -channel production of ZZ . Therefore, any deviation from the tree-level SM predictions will indicate the presence of beyond SM (BSM) physics. Although the interference of the dimension-8 operator with the SM contributes to the amplitude at $\mathcal{O}(1/\Lambda^4)$, the quadratic contribution of the dimension-6 operators does not need to be considered for the process of $e^+e^- \rightarrow ZZ$, as no dimension-6 operator contributes to the nTGCs.

The scattering process at the positron collider can be enhanced or reduced by the initial beam polarization. The hard bremsstrahlung cross section for polarized $e^+e^- \rightarrow ZZ$ scattering can be obtained as,

$$\begin{aligned}
\sigma_{\text{pol}}^{\text{SM}}(ZZ) &= - \left(16s_W^8 (P_{e^+} + 1)(P_{e^-} - 1) + (1 - 2c_W^2)^4 (P_{e^+} - 1)(P_{e^-} + 1) \right) \\
&\quad \times \frac{e^4 \left(\sqrt{s(s - 2M_Z^2)} \sqrt{s - 4M_Z^2} - (4M_Z^4 + s^2) \tanh^{-1} \left(\frac{\sqrt{s}\sqrt{s - 4M_Z^2}}{s - 2M_Z^2} \right) \right)}{128\pi c_W^4 s^2 s_W^4 (2M_Z^2 - s)}, \\
\sigma_{\text{pol}}^{\text{int}}(ZZ) &= \left(4(c_W^2 - 1)(P_{e^+} + 1)(P_{e^-} - 1)s_W^2 + (1 - 2c_W^2)^2 (P_{e^+} - 1)(P_{e^-} + 1) \right) \\
&\quad \times \frac{f_{\tilde{B}W} e^2 M_Z^2 \left(\sqrt{s(2M_Z^2 + s)} \sqrt{s - 4M_Z^2} - 4M_Z^2 (s - M_Z^2) \tanh^{-1} \left(\frac{\sqrt{s}\sqrt{s - 4M_Z^2}}{s - 2M_Z^2} \right) \right)}{32\pi c_W s^2 s_W}, \\
\sigma_{\text{pol}}^{\text{nTGC}}(ZZ) &= - \frac{f_{\tilde{B}W}^2 c_W^2 M_Z^2 s_W^2 (s - 4M_Z^2)^{\frac{5}{2}} (P_{e^-} - P_{e^+} - 1)}{24\pi\sqrt{s}}. \quad (2.2)
\end{aligned}$$

where P_{e^-} and P_{e^+} denote the polarization parameter of electron and positron respectively, ranging from -1 to $+1$, with $+1$ (-1) for the left (right) handed helicity.

Table 1: Comparison of the hard bremsstrahlung cross section (fb) of the SM and nTGCs contributions for 100% polarized $e^-e^+ \rightarrow ZZ$ scattering at the characteristic c.m. energies of CEPC, ILC, and CLIC.

P_{e^-}, P_{e^+}		0, 0	-1, -1	-1, 1	1, -1	1, 1
$\sqrt{s} = 250$ GeV	nTGCs	4.50×10^{-3}	0	8.99×10^{-3}	8.99×10^{-3}	0
	SM	1050	0	2637	1564	0
$\sqrt{s} = 360$ GeV	nTGCs	0.06	0	0.12	0.12	0
	SM	627	0	1574	933	0
$\sqrt{s} = 500$ GeV	nTGCs	0.336	0	0.673	0.673	0
	SM	397	0	996	591	0
$\sqrt{s} = 1$ TeV	nTGCs	7.07	0	14.1	14.1	0
	SM	145	0	363	215	0
$\sqrt{s} = 3$ TeV	nTGCs	617	0	1234	1234	0
	SM	24.9	0	62.5	37.1	0

Numerical results are evaluated for two energy points and the following helicity fraction of the electron (P_{e^-}) and positron (P_{e^+}) beam polarization:

$$(P_{e^-}, P_{e^+}) = (0, 0), (-1, -1), (-1, +1), (+1, -1), (+1, +1). \quad (2.3)$$

It is convenient to make a comparison of the cross sections induced by the SM couplings and nTGCs with different values of polarization in Table 1. The results are calculated with $f_{\hat{B}W} = 1$ (TeV^{-4}) as the characteristic parameter. The e^+e^- colliders will be constructed in several centre-of-mass (c.m.) energy stages, 250 GeV, 360 GeV, 500 GeV, 1 TeV and 3 TeV for two stages of CEPC and ILC, as well as CLIC, respectively. For each energy, the cross section of contributions of nTGCs $\sigma_{--,++}$ is 0, and σ_{+-} or σ_{-+} is all about 2 times larger than the unpolarized cross section. For the SM contributions, σ_{+-} is about 1.5 times larger than the unpolarized cross section.

Figure 2 shows the effects of initial beam polarization on cross sections at the various proposed e^+e^- colliders, based on a simple signal significance analysis with

$$S_{stat}(ZZ) = \frac{\sigma_{\text{pol}}^{\text{nTGC}} + \sigma_{\text{pol}}^{\text{int}}}{\sqrt{\sigma_{\text{pol}}^{\text{nTGC}} + \sigma_{\text{pol}}^{\text{int}} + \sigma_{\text{pol}}^{\text{SM}}}}. \quad (2.4)$$

It shows that beam polarization can improve significance by a factor of $1.4 \sim 2$ compared to the unpolarized process at the electron-positron colliders with a range of c.m. energy from 250 GeV to 3 TeV. The results have demonstrated the significance of polarization effects.

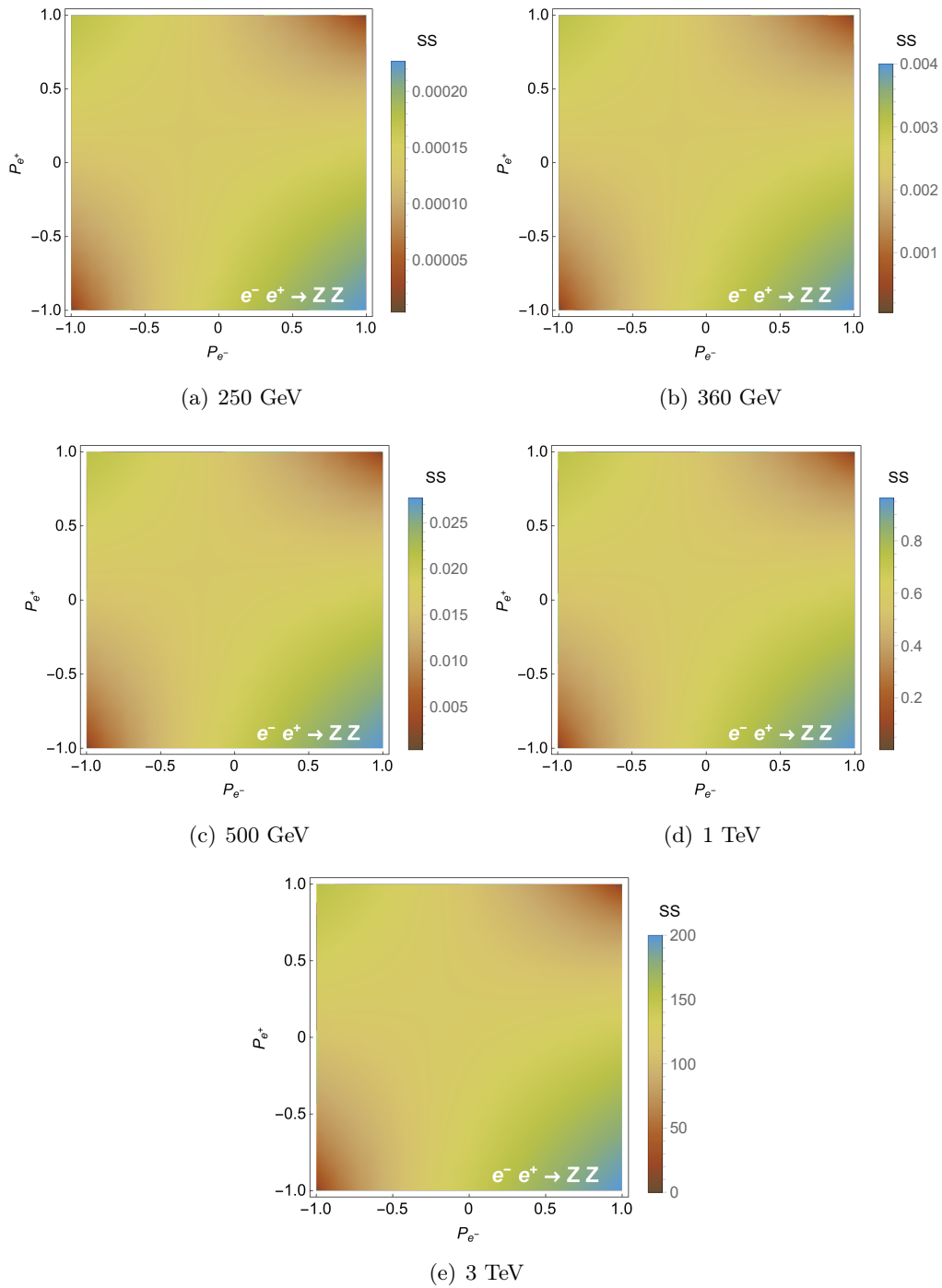


Figure 2: The statistical significance with $f_{\tilde{B}W} = 1$ (TeV^{-4}) and different beam polarization parameter for $\sqrt{s} = 250$ GeV, 360 GeV, 500 GeV, 1 TeV and 3 TeV, respectively.

Table 2: Summary of center-of-mass energies (\sqrt{s}) and corresponding integrated luminosities (\mathcal{L}) for different colliders.

Collider	Center-of-Mass Energy (\sqrt{s})	Integrated Luminosity (\mathcal{L})
CEPC	250 GeV	5 ab ⁻¹
CEPC	360 GeV	1 ab ⁻¹
ILC	500 GeV	500 fb ⁻¹
ILC	1 TeV	1 ab ⁻¹
CLIC	3 TeV	5 ab ⁻¹

3 Probing nTGCs via ZZ production at the future e^+e^- colliders

ZZ production processes can be further divided into five decay modes in the final states. In this analysis we study the following subprocesses:

$$e^+e^- \rightarrow Z_1(\ell^+\ell^-)Z_2(\ell^+\ell^-), \quad (3.1)$$

$$e^+e^- \rightarrow Z_1(jj)Z_2(jj), \quad (3.2)$$

$$e^+e^- \rightarrow Z_1(\ell^+\ell^-)Z_2(jj), \quad (3.3)$$

$$e^+e^- \rightarrow Z_1(\ell^+\ell^-)Z_2(\nu\bar{\nu}), \quad (3.4)$$

$$e^+e^- \rightarrow Z_1(jj)Z_2(\nu\bar{\nu}), \quad (3.5)$$

where ℓ is either e or μ . All processes are generated using `MadGraph5_aMC@NLO` toolkit [74, 75] with the LHCO output format; hadronization is performed by `PYTHIA8` [76]. A fast detector simulation is applied using `Delphes` [77] with the CEPC, ILC and two stages of CLIC collider cards. Finally, the events are reconstructed with the `MAnalysis` [78] package. All events simulated at future e^+e^- colliders will use an electron positron beam longitudinal polarisation of (+0.8, -0.8). Table 2 shows the integrated luminosities \mathcal{L} for the CEPC, ILC and CLIC at different stages of \sqrt{s} .

3.1 Selection of $e^+e^- \rightarrow 2\ell 2\ell'$

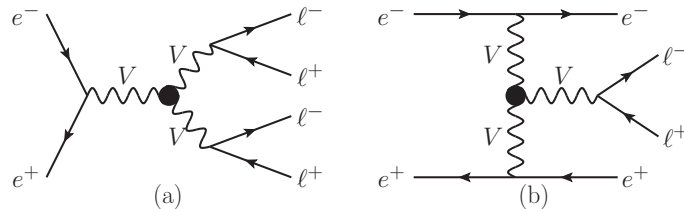


Figure 3: The Feynman diagrams of the nTGC contributions for the process $e^+e^- \rightarrow 2\ell 2\ell'$, where VVV stands for ZZZ , $ZZ\gamma$ or $Z\gamma\gamma$ couplings.

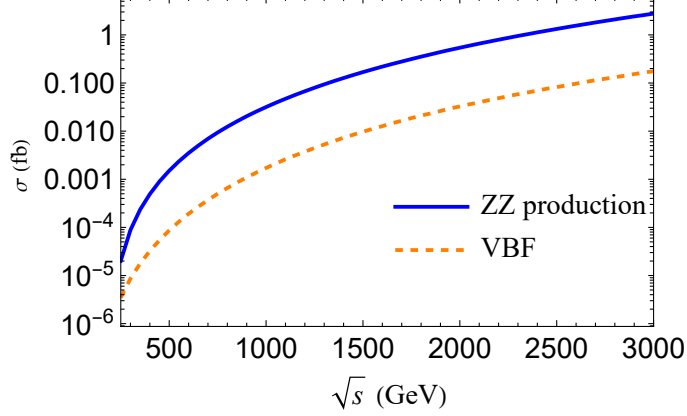


Figure 4: A comparison of σ_{diboson} and σ_{VBF} for $e^+e^- \rightarrow 2\ell 2\ell'$ as a function of \sqrt{s} with $f_{\hat{B}W} = 1$ (TeV^{-4}).

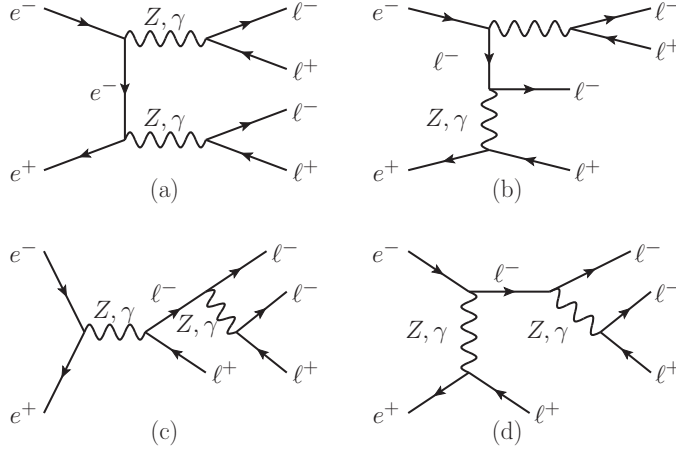


Figure 5: Typical Feynman diagrams of the SM backgrounds for the process $e^+e^- \rightarrow 2\ell 2\ell'$.

Z -pairs decaying to final states with four charged leptons ($\ell = e, \mu$) produce low multiplicity events with a clear topological signature that is exploited to maximize the selection efficiency. In addition to ZZ production, nTGCs can contribute to the $e^+e^- \rightarrow 2\ell 2\ell'$ process via di-boson production ($\gamma\gamma, Z\gamma$) and VBS processes, as shown in Fig. 3. Therefore, we need to compare the contribution of nTGC in the annihilation process and the VBS process. From Fig. 4, di-boson production dominates the signal above 10 times over the vector boson fusion (VBF) contribution for $e^+e^- \rightarrow 2\ell 2\ell'$. The annihilation process is more sensitive to the dimension-8 operators, so in signal and background analysis, the kinematic distributions of the nTGC signal will mainly refer to the characteristics of the annihilation process.

The corresponding Feynman diagrams of the SM backgrounds are shown in Fig. 5. The major contributions to the background are due to Z production in association with two isolated leptons, as shown in Fig. 5(b, c, d). The four-lepton final state from the di-boson production in the SM comes from the t -channel diagrams as Fig. 5(a).

Table 3: The ranges of coefficients $f_{\tilde{B}W}(\text{TeV}^{-4})$ used for each energy point in the MC simulation.

$\sqrt{s}=250$ GeV	$\sqrt{s}=360$ GeV	$\sqrt{s}=500$ GeV	$\sqrt{s}=1000$ GeV	$\sqrt{s}=3000$ GeV
$[-100, 100]$	$[-100, 100]$	$[-10, 10]$	$[-2.0, 2.0]$	$[-0.15, 0.15]$

Variables used in this analysis include the transverse momentum $p_T = \sqrt{p_x^2 + p_y^2}$ and the pseudorapidity defined in terms of the polar angle θ as $\eta = -\ln[\tan(\theta/2)]$. The basic cuts are set as same as the default settings of `MadGraph5_aMC@NLO`, except for $\Delta R_{\ell\ell}$ which is defined as $\sqrt{\Delta\eta_{\ell\ell}^2 + \Delta\phi_{\ell\ell}^2}$ where $\Delta\eta_{\ell\ell}$ and $\Delta\phi_{\ell\ell}$ are the differences between pseudo-rapidities and azimuth angles of the leptons, respectively. In the basic cuts we use $\Delta R_{\ell\ell} > 0.2$ [79] as configurations with collinear leptons are excluded. In the MC simulation, we use the coefficients in the ranges listed in Table 3.

To study the kinematic features of the signal and background, We adopt the conventional approach of considering one operator at a time, as is widely used in analyses within the SMEFT framework. The largest coefficients in Table 3 are adopted. We require at least four leptons in the 4ℓ signal mode. All the numerical results are presented after lepton number cut $N_\ell \geq 4$ (denoted as N_ℓ cut).

For the SM diagram in Fig. 5(a), we expect that the distribution of SM background events is dominantly around small t and thus the transverse momentum of one of the vectors is small. Denoting p_T^ℓ as the transverse momentum of the hardest lepton and E_{cm} as the c.m. energy, the normalized distributions of p_T^ℓ/E_{cm} for the signal of $\mathcal{O}_{\tilde{B}W}$ and the background are displayed in Fig. 6. The leptons from the SM background are softer than those from the nTGC signal. In addition, we also checked the η^ℓ distribution of the final state leptons. At low energies, the scattering angle of low-energy particles is smaller, and the direction of motion of the final-state leptons is more forward. At high energies, the scattering of high-energy particles will cause the final-state leptons to be more widely distributed in different directions. The distribution of η^ℓ of the signal will approach the SM background with the increase of the collision energy. Therefore, we did not use η^ℓ as the cut in the signal background analysis for CLIC. The angle between the same sign leptons $\cos\theta_\ell$ is used at high energy. At high energies, the direction of the lepton is approximately consistent with that of the highly boosted Z , so the angle between leptons of the same sign is approximately the angle between two parent particles. The dominate contribution of nTGCs is through s -channel of the di-boson diagrams. Therefore, the angular distributions of di-boson production induced by nTGCs and the SM should be different.

Since the main contribution to the signal comes from the di-boson production, the SM background from mono Z or γ production can be suppressed by requiring the event to contain two reconstructed Z bosons. $M_{Z_1}^{\text{rec}}$ and $M_{Z_2}^{\text{rec}}$ represent individually the reconstructed invariant mass of the first pair and the second pair of leptons. The distributions of $M_{Z_1}^{\text{rec}}$ and $M_{Z_2}^{\text{rec}}$ in Fig. 6 exhibit peaks around the mass of the Z boson for the signal. Most background events reconstruct $M_{Z_1}^{\text{rec}}$, but do not work well for reconstructing $M_{Z_2}^{\text{rec}}$. The joint requirement of the invariant mass of the reconstructed $Z_{1,2}$ is required to

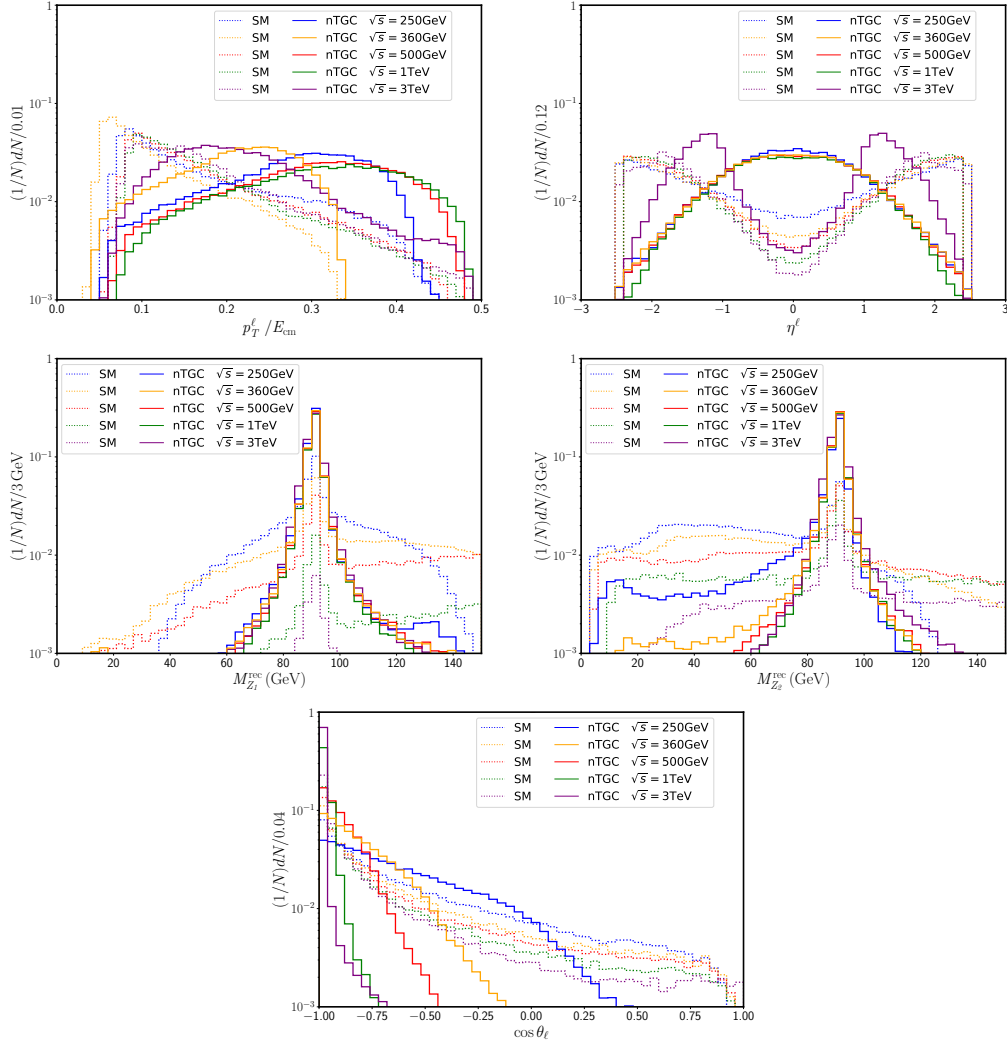


Figure 6: The normalized distributions of p_T^ℓ/E_{cm} , η^ℓ , $M_{Z_1}^{\text{rec}}$, $M_{Z_2}^{\text{rec}}$ and $\cos\theta_\ell$ for $e^+e^- \rightarrow 2\ell 2\ell'$.

Table 4: The event selection strategy and cross sections (fb) after cuts for each energy point. The results of nTGCs are obtained using the upper bounds of the coefficients in Table 3.

	$\sqrt{s}=250$ GeV		$\sqrt{s}=360$ GeV		$\sqrt{s}=500$ GeV		$\sqrt{s}=1$ TeV		$\sqrt{s}=3$ TeV	
	SM	NP	SM	NP	SM	NP	SM	NP	SM	NP
Basic Cuts	22.83	0.254	16.50	3.015	11.64	0.161	5.301	0.109	1.336	0.022
$p_T^\ell/E_{\text{cm}} > 0.15$	11.01	0.228	7.387	2.719						
$p_T^\ell/E_{\text{cm}} > 0.2$					3.584	0.133	1.555	0.092		
$ \eta^\ell < 1.5$	9.244	0.225	5.712	2.652	3.519	0.133	1.502	0.092		
$\cos\theta_\ell < 0.4$	8.882	0.225								
$\cos\theta_\ell < -0.2$			4.909	2.620						
$\cos\theta_\ell < -0.6$					2.534	0.130	1.102	0.092	1.060	0.022
$ M_{Z_1, Z_2}^{\text{rec}} - M_Z < 10$ GeV	2.460	0.157	0.976	2.074	0.361	0.104	0.079	0.073	0.014	0.016
Efficiency ϵ	6.8%	40%	3.5%	43%	1.8%	40%	0.8%	40%	0.6%	53%

satisfy $80 < M_{\ell\ell} < 100$ GeV, which can effectively suppress the background events from Fig. 5(b,c,d). However, other kinematic observable measurements are needed to further optimize the event screening strategy to eliminate the background from Fig. 5(a). Table 4 shows the cross sections with event selection strategy and cut efficiencies obtained in all energy cases.

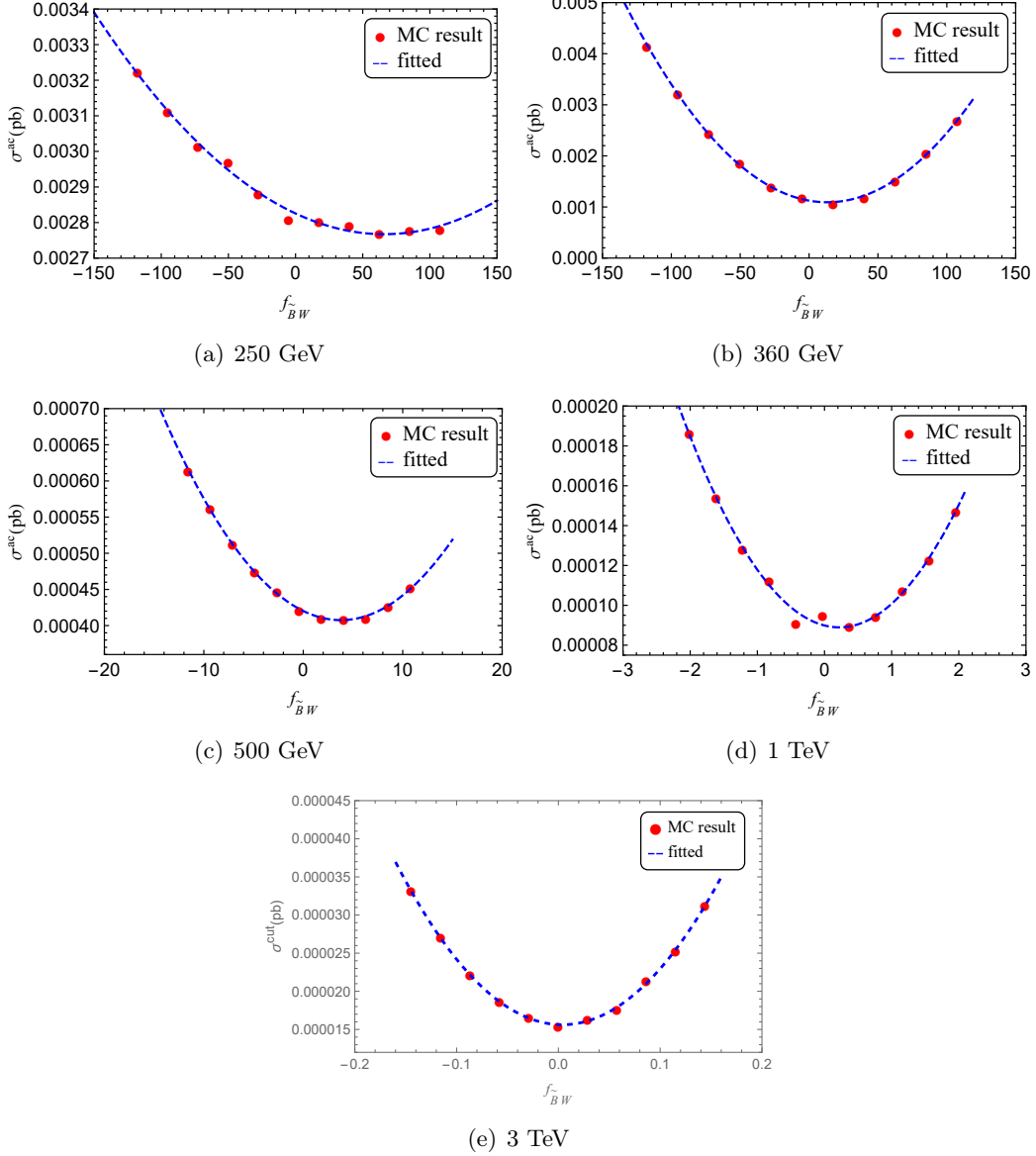


Figure 7: Cross sections as function of $f_{\tilde{B}W}$ (TeV^{-4}) for $e^+e^- \rightarrow 2\ell 2\ell'$.

The total cross sections after event selection strategy (denoted by $\sigma_{\text{nTGC}}^{\text{ac}}$) are obtained by scanning some values of coefficient with $\mathcal{O}_{\tilde{B}W}$, and shown in Fig. 7. Taking into account the impact of interference terms, the cross sections $\sigma_{\text{nTGC}}^{\text{ac}}$ can be fitted as bilinear functions

of $f_{\tilde{B}W}$ (TeV^{-4}), as

$$\sigma_{\text{nTGC}}^{\text{ac}} = \epsilon_{\text{SM}}\sigma_{\text{SM}} + f_{\tilde{B}W}^2\sigma_{\text{NP}}^{\text{ac}} + f_{\tilde{B}W}\hat{\sigma}_{\text{int}}, \quad (3.6)$$

where ϵ_{SM} and ϵ_{NP} are the cut efficiencies of SM and nTGC events, respectively, which are listed in Table 4. $\sigma_{\text{NP}}^{\text{ac}}$ is NP contribution after cuts to be fitted and $\hat{\sigma}_{\text{int}}$ is the interference parameter to be fitted. The numerical results of efficiencies are given in Table 4. The fitted results of $\hat{\sigma}_{\text{int}}$ can then be obtained and are given in Table 5.

Table 5: The fitted values of $\sigma_{\text{NP}}^{\text{ac}}$ ($\text{fb} \times \text{TeV}^8$) and $\hat{\sigma}_{\text{int}}$ ($\text{fb} \times \text{TeV}^4$) for each energy point, where $\sigma_{\text{NP}}^{\text{ac}}$ and $\hat{\sigma}_{\text{int}}$ is defined in Eq. (3.6).

\sqrt{s}	250 GeV	360 GeV	500 GeV	1 TeV	3 TeV
$\hat{\sigma}_{\text{int}}$	-0.0018	-0.0048	-0.0067	-0.0085	-0.0062
$\sigma_{\text{NP}}^{\text{ac}}$	0.00001	0.0002	0.0008	0.0194	0.7942

The sensitivity of the future e^-e^+ colliders to the nTGC operators and the expected constraints on the coefficients can be obtained with respect to the significance defined as [80, 81]

$$\mathcal{S}_{\text{stat}} = \sqrt{2[(N_{\text{bg}} + N_s)\ln(1 + N_s/N_{\text{bg}}) - N_s]}, \quad (3.7)$$

where $N_s = N_{\text{nTGC}} - N_{\text{SM}}$ and $N_{\text{bg}} = N_{\text{SM}}$. The likelihood function for N_s is defined as

$$L(N_s) = \frac{(N_{\text{bg}} + N_s)^n}{n!} e^{-(N_{\text{bg}} + N_s)}, \quad (3.8)$$

and one can find the maximum by setting $\partial \ln L / \partial N_s = 0$. The approximate significance is then obtained by taking the square root of the likelihood ratio statistic $-2\ln(L(0)/L(N_s))$ after letting $n = N_{\text{bg}} + N_s$ [80]. The number of events N_{nTGC} is obtained by setting certain high-dimensional coefficient $f_{\tilde{B}W}$ in SMEFT. The number of background events N_{SM} denotes the SM prediction with the high-dimensional coefficient vanishing.

As a result, we can obtain the projected sensitivity on $f_{\tilde{B}W}$ by taking 2σ , 3σ or 5σ significance. The results are shown in Table 6.

Table 6: The expected constraints on $f_{\tilde{B}W}$ (TeV^{-4}) for $e^+e^- \rightarrow 2\ell 2\ell'$ at each energy point of CEPC, ILC and CLIC with corresponding design luminosities.

$\mathcal{S}_{\text{stat}}$	\sqrt{s} (GeV)				
	250	360	500	1000	3000
2	[-23.1, 155.0]	[-10.4, 36.9]	[-5.4, 13.0]	[-0.84, 1.28]	[-0.088, 0.096]
3	[-32.8, 164.6]	[-14.3, 40.8]	[-7.3, 14.9]	[-1.11, 1.55]	[-0.114, 0.121]
5	[-49.9, 181.8]	[-21.1, 47.5]	[-10.7, 18.2]	[-1.57, 2.01]	[-0.160, 0.169]

3.2 Selection of $e^+e^- \rightarrow 4j$

The hadronic selection of ZZ production is very important, which represents 49% of the ZZ decay topologies. The signal is characterized by four or more jets in the final state, and the contribution to the signal is not only the pair production of Z boson, but also the W boson. $e^+e^- \rightarrow 4j$ channel has only one topology induced by 5 electroweak vertices ZZZ , $Z\gamma\gamma$, $ZZ\gamma$, WWZ and $WW\gamma$. At tree level, the Feynman diagram is shown in Fig. 8. The background include reducible contributions from QCD processes and di-boson productions. Fig. 9 shows the typical Feynman diagrams.

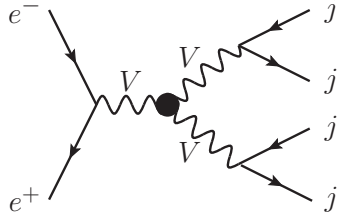


Figure 8: The signal Feynman diagrams for the process $e^+e^- \rightarrow 4j$, where VVV stands for ZZZ , $ZZ\gamma$, $Z\gamma\gamma$, ZWW or γWW couplings.

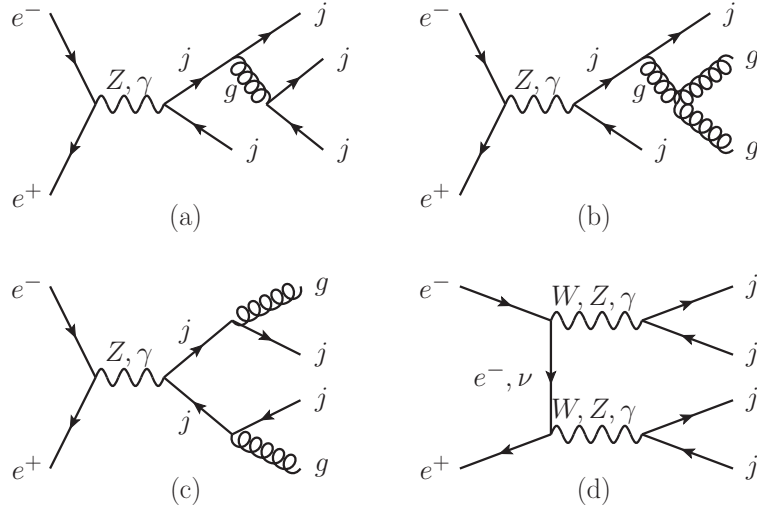


Figure 9: The background Feynman diagrams for the process $e^+e^- \rightarrow 4j$.

The event selection strategy is optimized separately for each energy point of future e^+e^- colliders. The basic cuts are the requirements of the isolated jet. A four-jet event sample is formed by requiring the jet resolution parameter are transverse momentum $p_T^j > 20$ GeV and pseudo-rapidity $\eta_j < 5.0$. Consider collinear jets from the same pairing at high energy scale, signal and background events required the number of jets of $N_j \geq 2$. Furthermore, the signal events are required to have at least two $V \rightarrow jj$ candidate ($V = W^\pm, Z$), denoted by V_1 and V_2 . The invariant masses of the two sets of di-jets, M_{V_1} and M_{V_2} , are reconstructed by the circular pairing, and then evaluating the mass difference

$\Delta_M = |M_{jj} - M_V|$ between each pairing and the vector boson. Δ_M will be calculated twice depending on whether M_V takes W mass or Z mass, The pairing scheme with the smallest sum of Δ_M for V_1 and V_2 is selected, and the mass window of M_{V_1} and M_{V_2} is used as the improved cuts to discriminate the QCD background events against the signal events of hadronic vector boson-pair events. The invariant mass distributions of the signal exhibit distinct peaks within the mass range of the W and Z bosons, as shown in figures 10. The distributions of M_{V_1} and M_{V_2} display small peaks around 15 GeV and 10 GeV, respectively, which could be attributed to $Z\gamma^*$ and $\gamma^*\gamma^*$ production. Considering that $Z\gamma$ production constitutes a minor portion of the signal and that background events dominate the low-energy region for M_{V_1} and M_{V_2} , we require that both M_{V_1} and M_{V_2} of the signal event satisfy the invariant mass range of the massive vector boson. We apply a mass window cut of $60 < M_{V_1, V_2} < 110$ GeV to ensure that the selected events consist of 4 jets from W and Z boson pair production induced by nTGC. The invariant mass selection aims for an inclusive selection of fully hadronic vector boson-pair decays.

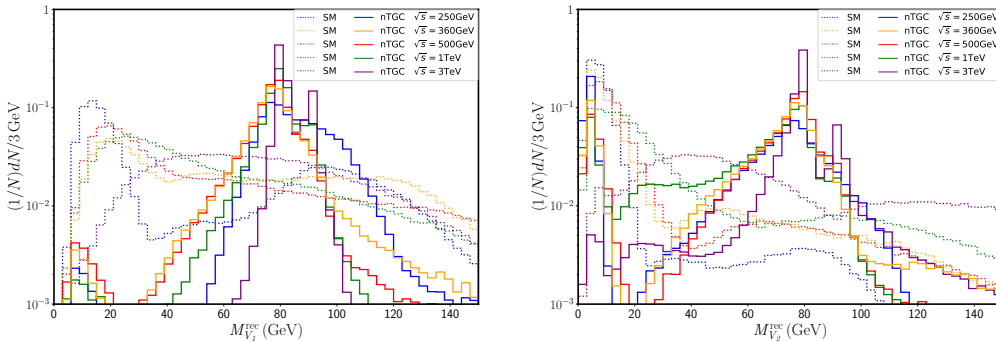


Figure 10: The normalized distributions of $M_{V_1}^{\text{rec}}$, $M_{V_2}^{\text{rec}}$ for $e^+e^- \rightarrow 4j$.

The specific values of event selection strategy and the respective cut efficiencies are presented in Table 7. With the cut flow applied, the total cross sections are obtained by scanning the values of coefficient with $\mathcal{O}_{\tilde{B}W}$, and the fitting functions are shown in Fig. 11. The fitting coefficients of interference terms are given in Table 8.

Table 7: The cross sections σ_{SM} and σ_{nTGC} of $e^+e^- \rightarrow 4j$ (in unit of fb) and cut efficiencies after event selection strategy.

	$\sqrt{s}=250$ GeV		$\sqrt{s}=360$ GeV		$\sqrt{s}=500$ GeV		$\sqrt{s}=1$ TeV		$\sqrt{s}=3$ TeV	
	SM	NP	SM	NP	SM	NP	SM	NP	SM	NP
Basic Cuts	2898	2.216	251.5	23.28	2103	1.684	994.2	1.655	208.1	0.988
$M_{V_1, V_2}^{\text{rec}} \in (60, 110)$ GeV	103.5	1.156	14.50	14.05	78.73	1.127	42.67	0.925	52.67	0.911
Efficiency ϵ	3.6%	52%	1.6%	60%	3.7%	67%	4.3%	55%	25%	92%

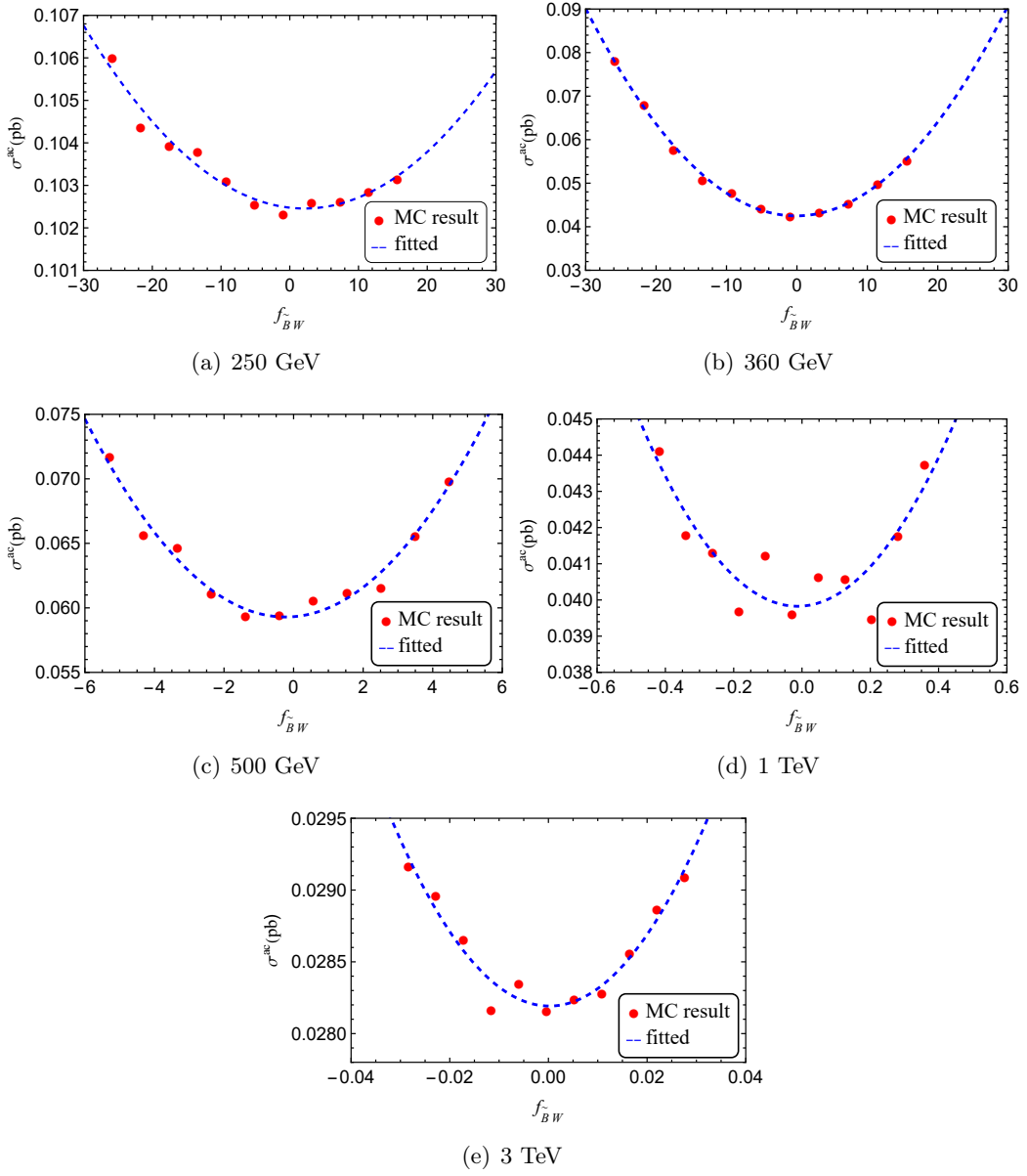


Figure 11: Cross sections as functions of $f_{\tilde{B}W}^c$ (TeV^{-4}) for $e^+e^- \rightarrow 4j$.

Table 8: The fitted values of $\sigma_{\text{NP}}^{\text{ac}}$ ($\text{fb} \times \text{TeV}^8$) and $\hat{\sigma}_{\text{int}}$ ($\text{fb} \times \text{TeV}^4$) for $e^+e^- \rightarrow 4j$ at each energy point, where $\sigma_{\text{NP}}^{\text{ac}}$ and $\hat{\sigma}_{\text{int}}$ is defined in Eq. (3.6).

\sqrt{s}	250 GeV	360 GeV	500 GeV	1 TeV	3 TeV
$\hat{\sigma}_{\text{int}}$	-0.0178	-0.0112	-0.2134	-0.1332	-0.5256
$\sigma_{\text{NP}}^{\text{ac}}$	0.0042	0.0533	0.4614	2.0408	1268.4

The sensitivities for the $e^+e^- \rightarrow 4j$ channel at the future e^+e^- colliders and the

expected constraints on the coefficients, as obtained with Eq. 3.7. The integrated luminosity \mathcal{L} is based on the design values of the CEPC, ILC and CLIC at four energies. The projected sensitivity on $f_{\tilde{B}W}$ by taking 2σ , 3σ or 5σ significance levels. The results are presented in Table 9. While the hadronic modes are considerably more challenging, the $4j$ signal channel at the e^+e^- colliders exhibits a high degree of sensitivity to the $\mathcal{O}_{\tilde{B}W}$ operators, which are even more pronounced than the four charged leptons mode.

Table 9: The expected constraints on $f_{\tilde{B}W}$ (TeV^{-4}) for $e^+e^- \rightarrow 4j$.

S_{stat}	\sqrt{s} (GeV)				
	250	360	500	1000	3000
2	[-6.4, 10.7]	[-2.7, 2.9]	[-1.0, 1.5]	[-0.15, 0.22]	[-0.011, 0.011]
3	[-8.2, 12.5]	[-3.3, 3.5]	[-1.3, 1.8]	[-0.20, 0.26]	[-0.013, 0.014]
5	[-11.2, 15.4]	[-4.3, 4.4]	[-1.7, 2.2]	[-0.27, 0.33]	[-0.017, 0.017]

3.3 Selection of $e^+e^- \rightarrow 2\ell 2j$

The signal of $2\ell 2j$ induced by nTGCs are composed of both VBS and di-boson production topologies with the decay of massive EW gauge bosons. The signal from ZZ production is the main component of nTGCs signal, which has a branching ratio in ZZ production of 4.7% per lepton flavour. The kinematic characteristics of ZZ decay products will provide the main feature of nTGC signal. The SM background can be divided into three categories according to whether the final-state leptons and jets can reconstruct Z . The typical Feynman diagrams of signal and background are shown in Fig. 12 and Fig. 13. The on-shell ZZ event can be selected by applying simultaneous cuts on the masses of the $\ell^+\ell^-$ pair, on the remaining hadronic system and on their sum.

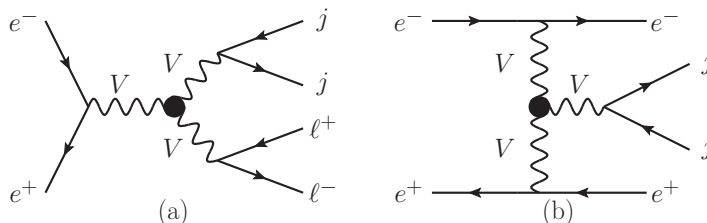


Figure 12: Typical Feynman diagrams which contribute to the process $e^+e^- \rightarrow 2\ell 2j$ for signal events, where VVV stands for ZZZ , $ZZ\gamma$ or $Z\gamma\gamma$ couplings.

As in the previous analysis, the signal events are generated by assuming one operator at a time, using the largest coefficients from Table 3. In the following studies, we require at least two leptons and two jets. All numerical results are presented after applying the particle number cuts: $N_{\ell^+} \geq 1$, $N_{\ell^-} \geq 1$, and $N_j \geq 2$, and the two hardest leptons be a lepton and an anti-lepton of the same flavor. This requirement is denoted as the $N_{\ell,j}$ cut.

Another important factor is $\Delta R_{\ell\ell}$ and ΔR_{jj} . When the Z boson is energetic, the leptons tend to be collinear, resulting in a small $\Delta R_{\ell\ell}$ and a small ΔR_{jj} for the signal events.

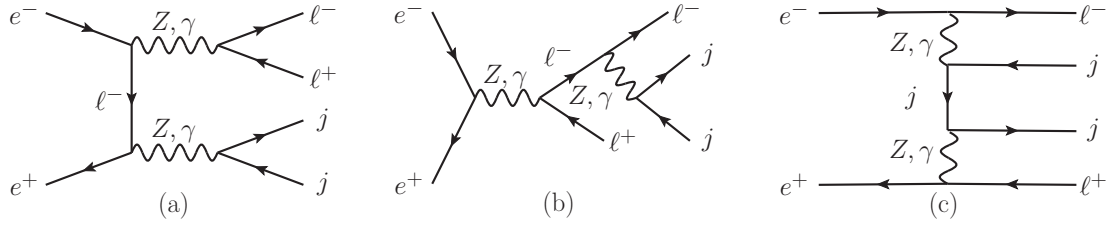


Figure 13: Typical Feynman diagrams which contribute to the process $e^+e^- \rightarrow 2\ell 2j$ for background events.

However, since $\Delta R_{\ell\ell}$ is related to lepton isolation, we impose a basic cut of $\Delta R_{\ell\ell} > 0.2$, which can be achieved in experiments [44].

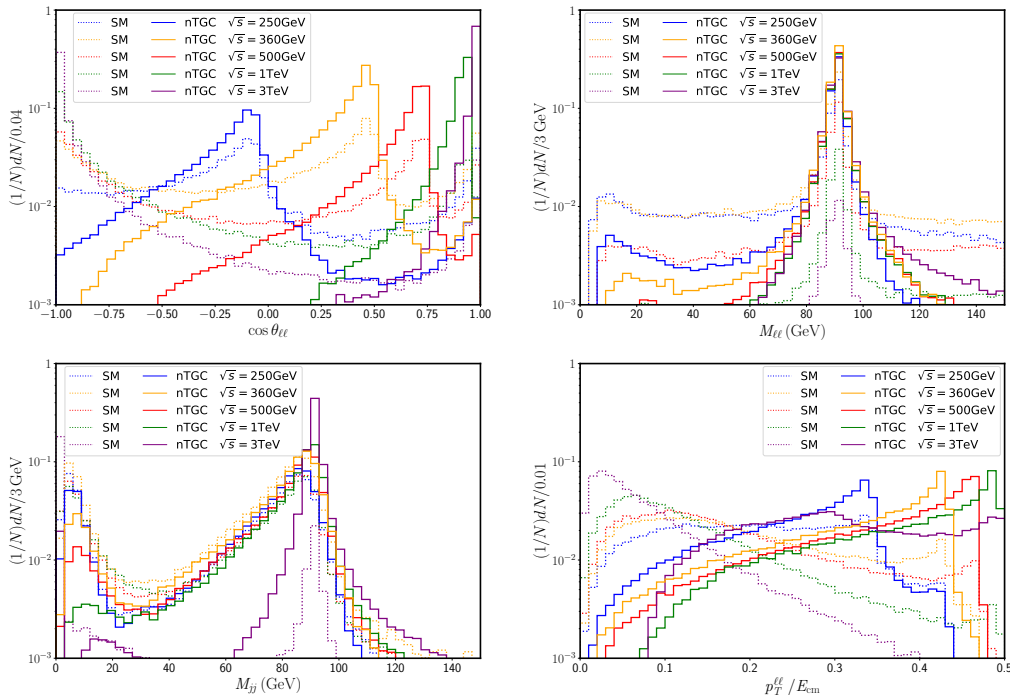


Figure 14: The normalized distributions of $\cos \theta$, $M_{\ell\ell}$, M_{jj} , $p_T^{\ell\ell}/E_{\text{cm}}$ for $e^+e^- \rightarrow 2\ell 2j$.

To remove the backgrounds without a Z resonance, we require the invariant mass of the leptons and jets, denoted as $M_{\ell\ell}$ and M_{jj} , to be close to M_Z . For events in the $\ell^+\ell^-jj$ final states, the Z direction was taken to be the direction of the reconstructed di-jet or $\ell^+\ell^-$ pair, respectively. The normalized distributions of $M_{\ell\ell}$ and M_{jj} are shown in Fig. 14. In the distributions of the signal, the peaks at M_Z are much sharper than those in the distributions of the SM backgrounds. We cut off the events with the mass window cut $70 < M_{\ell\ell} < 110$ GeV. It should be noted that in the case of $\sqrt{s} = 250$ and 360 GeV, $M_{\ell\ell}$ has a resonance peak mainly from the $Z\gamma^*$ production processes at about 10 GeV. For CEPC, the mass window cut increases the range by an additional $5 < M_{\ell\ell} < 20$ GeV. The M_{jj} distributions for the nTGC signal and the SM background show similarity at

low energies. However, these distributions become more distinguishable at higher energies. Consequently, we included M_{jj} as a selection criterion only in the 3 TeV analysis.

After applying $M_{\ell\ell,jj}$ cut, the SM backgrounds in Fig. 13 (b,c) can be excluded, leaving the events from Fig. 13 (a). The dominate contribution of nTGCs is through s -channel of the di-boson diagram, Fig. 12 (a). In the signal event, leptons and jets come from the decay of bosons emitted in the s -channel diagram. We expect the leptons and jets in the signal to be more energetic than those in the background, and anticipate the same for their parent particle, the reconstructed Z boson. Thus $p_T^{\ell\ell}/E_{\text{cm}}$ will work for this channel. At high energies, the direction of the lepton or jet is approximately consistent with that of the highly boosted Z . Therefore, in the c.m. frame, the angle $\theta_{\ell\ell}$ between the two leptons in signal are different from those in background as shown in Fig. 14. We cut off the events with a large $\cos\theta_{\ell\ell}$ at high energy scale. This effect is not obvious on CEPC with lower c.m. energy, but the signal selection efficiency can still be slightly improved by a cut of $-0.6 < \cos\theta < 0.2$. The specific values of event selection strategy and the respective cut efficiencies are presented in Table 10.

Table 10: The event selection strategy and cross sections of $e^+e^- \rightarrow 2\ell 2j$ (in unit of fb) after cuts.

	$\sqrt{s}=250$ GeV		$\sqrt{s}=360$ GeV			
	SM	NP	SM	NP		
Basic Cuts	86.08	0.556	63.43	7.454		
$-0.7 < \cos\theta_{\ell\ell} < 0.2$	53.66	0.482				
$-0.5 < \cos\theta_{\ell\ell} < 0.7$			38.55	7.058		
$M_{\ell\ell} \in$ $(5, 20) \cup (70, 110)$ GeV	47.79	0.471	30.21	6.814		
$p_T^{\ell\ell}/E_{\text{cm}} > 0.1$	40.95	0.440	23.52	6.540		
Efficiency ϵ	35%	60%	27%	68%		
	$\sqrt{s}=500$ GeV		$\sqrt{s}=1$ TeV		$\sqrt{s}=3$ TeV	
	SM	NP	SM	NP	SM	NP
Basic Cuts	52.08	0.484	25.69	0.430	11.35	0.162
$\cos\theta_{\ell\ell} > 0$	25.79	0.460	6.724	0.426		
$\cos\theta_{\ell\ell} > 0.5$					0.898	0.157
$M_{\ell\ell} \in (70, 110)$ GeV	17.54	0.436	3.187	0.402		
$M_{\ell\ell,jj} \in (70, 110)$ GeV					0.334	0.134
$p_T^{\ell\ell}/E_{\text{cm}} > 0.3$	5.305	0.312	1.084	0.305		
$p_T^{\ell\ell}/E_{\text{cm}} > 0.1$					0.325	0.133
Efficiency ϵ	7.4%	51%	2.9%	54%	2.1%	71%

With the event selection strategy of $e^+e^- \rightarrow 2\ell 2j$ applied, the total cross sections are

obtained by scanning the values of coefficient with $\mathcal{O}_{\tilde{B}W}$, and the fitting functions are shown in Fig. 15. The fitting coefficients of interference terms are given in Table 11.

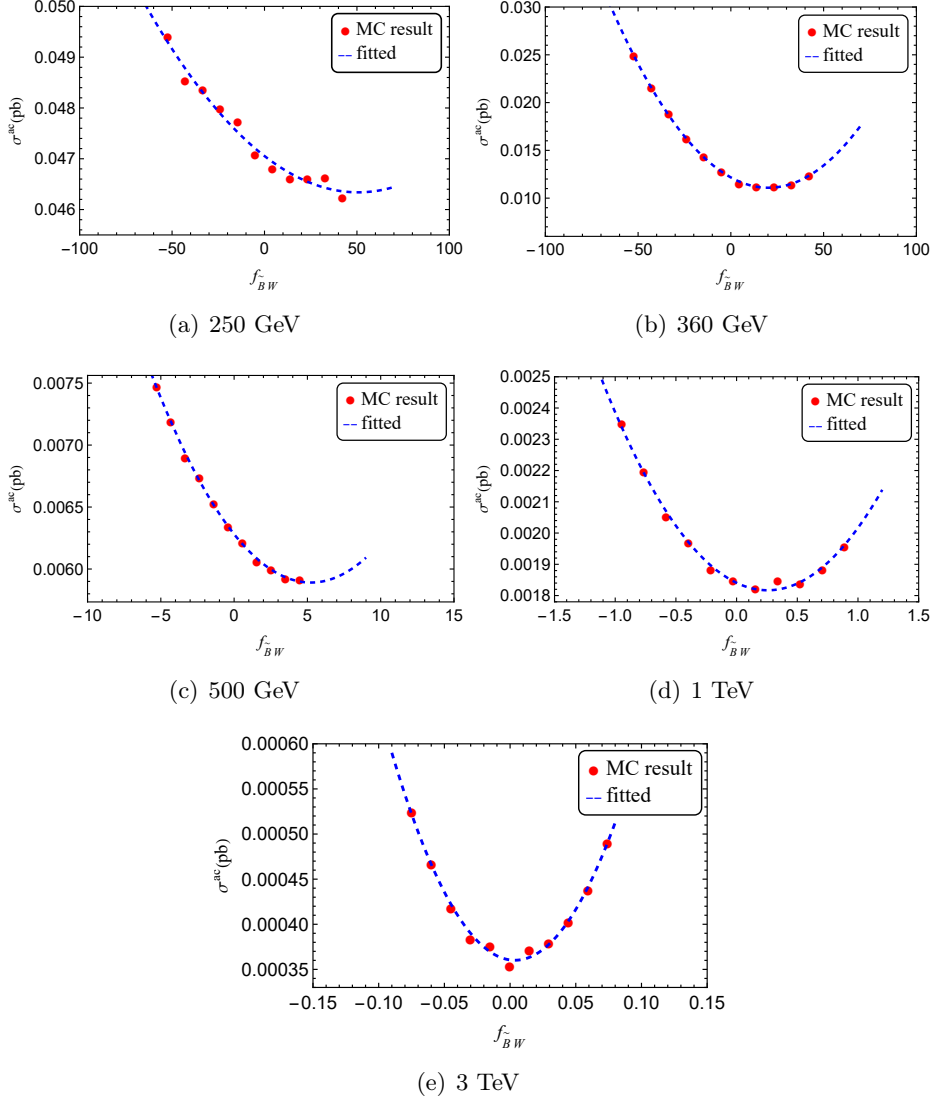


Figure 15: Cross sections as functions of $f_{\tilde{B}W}$ (TeV^{-4}) for $e^+e^- \rightarrow 2\ell 2j$.

Table 11: The fitted values of $\sigma_{\text{NP}}^{\text{ac}}$ ($\text{fb} \times \text{TeV}^8$) and $\hat{\sigma}_{\text{int}}$ ($\text{fb} \times \text{TeV}^4$) for $e^+e^- \rightarrow 2\ell 2j$ at each energy point, where $\sigma_{\text{NP}}^{\text{ac}}$ and $\hat{\sigma}_{\text{int}}$ is defined in Eq. (3.6).

\sqrt{s}	250 GeV	360 GeV	500 GeV	1 TeV	3 TeV
$\hat{\sigma}_{\text{int}}$	-0.0282	-0.1064	-0.1489	-0.1848	-0.1219
$\sigma_{\text{NP}}^{\text{ac}}$	0.0003	0.0026	0.0142	0.3607	24.179

The sensitivities for the $e^+e^- \rightarrow 2\ell 2j$ channel and the expected constraints on the

coefficients obtained with Eq. 3.7. We obtain the projected sensitivity on $f_{\tilde{B}W}$ by taking 2σ , 3σ or 5σ significance. The results are shown in Table 12.

Table 12: The expected constraints on $f_{\tilde{B}W}$ (TeV^{-4}) for $e^+e^- \rightarrow 2\ell 2j$.

S_{stat}	\sqrt{s} (GeV)				
	250	360	500	1000	3000
2	[-6.5, 107.7]	[-2.0, 42.5]	[-1.4, 11.8]	[-0.30, 0.81]	[-0.022, 0.030]
3	[-9.5, 110.7]	[-2.9, 43.4]	[-2.0, 12.4]	[-0.40, 0.92]	[-0.028, 0.036]
5	[-15.0, 116.3]	[-4.7, 45.2]	[-3.0, 13.5]	[-0.58, 1.09]	[-0.038, 0.045]

The lepton pairs in the $2\ell 2j$ final states have a distinctive signature making possible selections with high efficiencies and low background contaminations. In comparison to previous section, the $2\ell 2j$ has the most sensitive detection capability for $\mathcal{O}_{\tilde{B}W}$ operator in the high energy region.

3.4 Selection of $e^+e^- \rightarrow \ell^+\ell^-\nu\bar{\nu}$

The Feynman diagrams of the contribution induced by nTGCs to the process $e^+e^- \rightarrow \ell^+\ell^-\nu\bar{\nu}$ are given in the Fig. 16. The dominant signal is the di-boson contribution induced by nTGCs. The contribution from the VBF process is negligible compared to the bi-bosonic process. As shown in Fig. 17, the contribution from WW production is more significant than that from ZZ production. Therefore, in the analysis of signal and background, the $\ell^+\ell^-\nu\bar{\nu}$ signal will primarily reflect the kinematic distribution characteristics of WW and ZZ production.

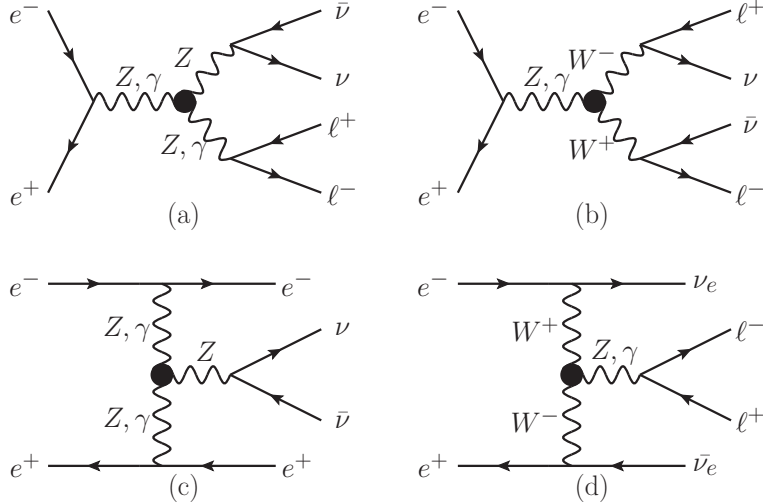


Figure 16: Typical Feynman diagrams which contribute to the process $e^+e^- \rightarrow \ell^+\ell^-\nu\bar{\nu}$ for signal events.

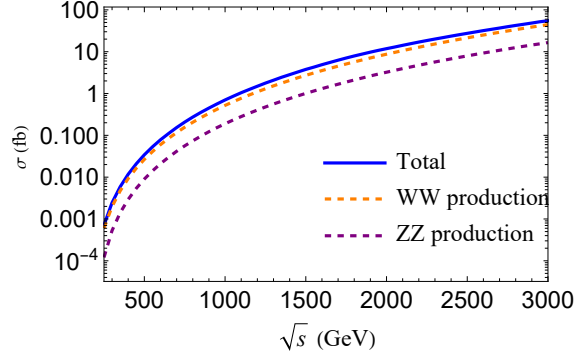


Figure 17: The comparison of σ_{Total} , σ_{WW} and σ_{ZZ} for $e^+e^- \rightarrow \ell\ell\nu\bar{\nu}$ as a function of c.m. energy \sqrt{s} with $f_{\tilde{B}W} = 1$ (TeV^{-4}).

The irreducible backgrounds in the $\ell^+\ell^-\nu\bar{\nu}$ channel arise from di-boson production (WW and ZZ), electroweak VBF and neutrino production in association with a vector boson that decays leptonically. The typical Feynman diagrams of the SM backgrounds are shown in Fig. 18. In order to suppress the SM backgrounds, the following basic cuts are used: $\Delta R_{\ell\ell} = 0.2$; $p_T^\ell = 10$ GeV; $N_\ell \geq 2$ and the two leptons must be a lepton and an anti-lepton of the same flavor. After these cuts, we further employ optimized kinematical cuts according to the kinematical distributions of the signal and background.

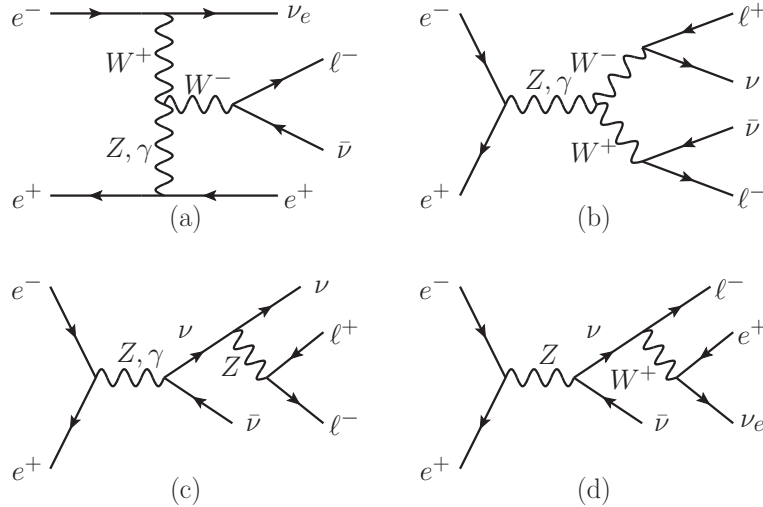


Figure 18: Typical Feynman diagrams which contribute to the process $e^+e^- \rightarrow \ell^+\ell^-\nu\bar{\nu}$ for background events.

In the event of two detectable leptons and invisible particles in the final state, the invariant mass, pseudorapidity, missing energy and reconstructed invariant mass can be extracted. We display the normalized distribution of these kinematic variables in Fig. 19 with the largest coefficients listed in Table 3. As the majority of leptons in the background are produced via radiation decay, it can be observed that the transverse momentum of these leptons is comparatively smaller than that of the signal. The Z boson is typically produced

in the central region in the nTGC process, and the leptons of Z decay are nearly collinear with the highly boosted Z , resulting in a relatively small distribution of pseudorapidity for the associated lepton. The candidate lepton is required to have $p_T^\ell > 0.2E_{\text{cm}}$, with $|\eta^\ell| < 1.5$ for CEPC and $|\eta^\ell| < 1$ for ILC and CLIC.

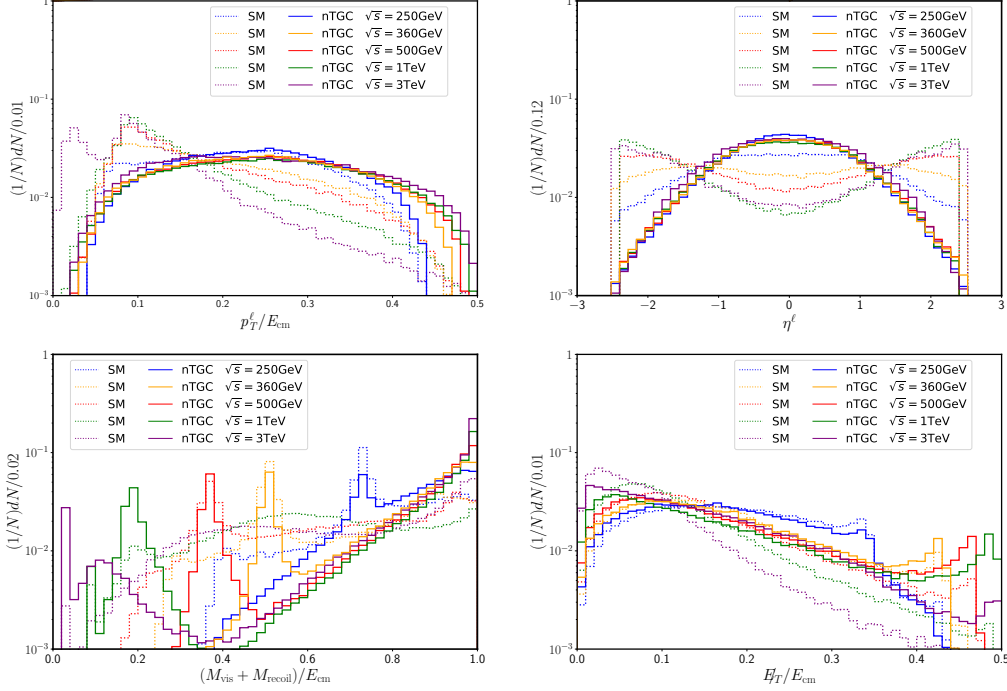


Figure 19: The normalized distributions of p_T^ℓ/E_{cm} , η^ℓ , $(M_{\text{vis}} + M_{\text{recoil}})/\sqrt{s}$ and E_T/\sqrt{s} for $e^+e^- \rightarrow \ell^+\ell^-\nu\bar{\nu}$.

Table 13: The event selection strategy and cross sections of $e^+e^- \rightarrow \ell^+\ell^-\nu\bar{\nu}$ (fb) after cuts.

	$\sqrt{s}=250$ GeV		$\sqrt{s}=360$ GeV			
	SM	NP	SM	NP		
Basic Cuts	87.72	12.03	62.04	86.36		
$ \eta^\ell < 1.5$	68.15	10.87	38.03	77.06		
$(M_{\text{vis}} + M_{\text{recoil}}) > 120\text{GeV}$	64.54	40.69	36.81	76.85		
Efficiency ϵ	59%	72%	46%	70%		
	$\sqrt{s}=500$ GeV		$\sqrt{s}=1$ TeV		$\sqrt{s}=3$ TeV	
	SM	NP	SM	NP	SM	NP
Basic Cuts	49.49	5.686	32.00	3.794	16.33	2.230
$p_T^\ell/E_{\text{cm}} > 0.2$	19.29	3.903	9.075	2.600	2.906	1.462
$ \eta^\ell < 1.0$	12.90	3.409	4.827	2.270	1.175	1.252
$(M_{\text{vis}} + M_{\text{recoil}}) \in$ $(150, 210)\text{GeV} \cup (0.7E_{\text{cm}}, E_{\text{cm}})$	9.625	3.117	2.719	2.002	0.584	1.129
Efficiency ϵ	15%	43%	6.4%	41%	2.7%	44%

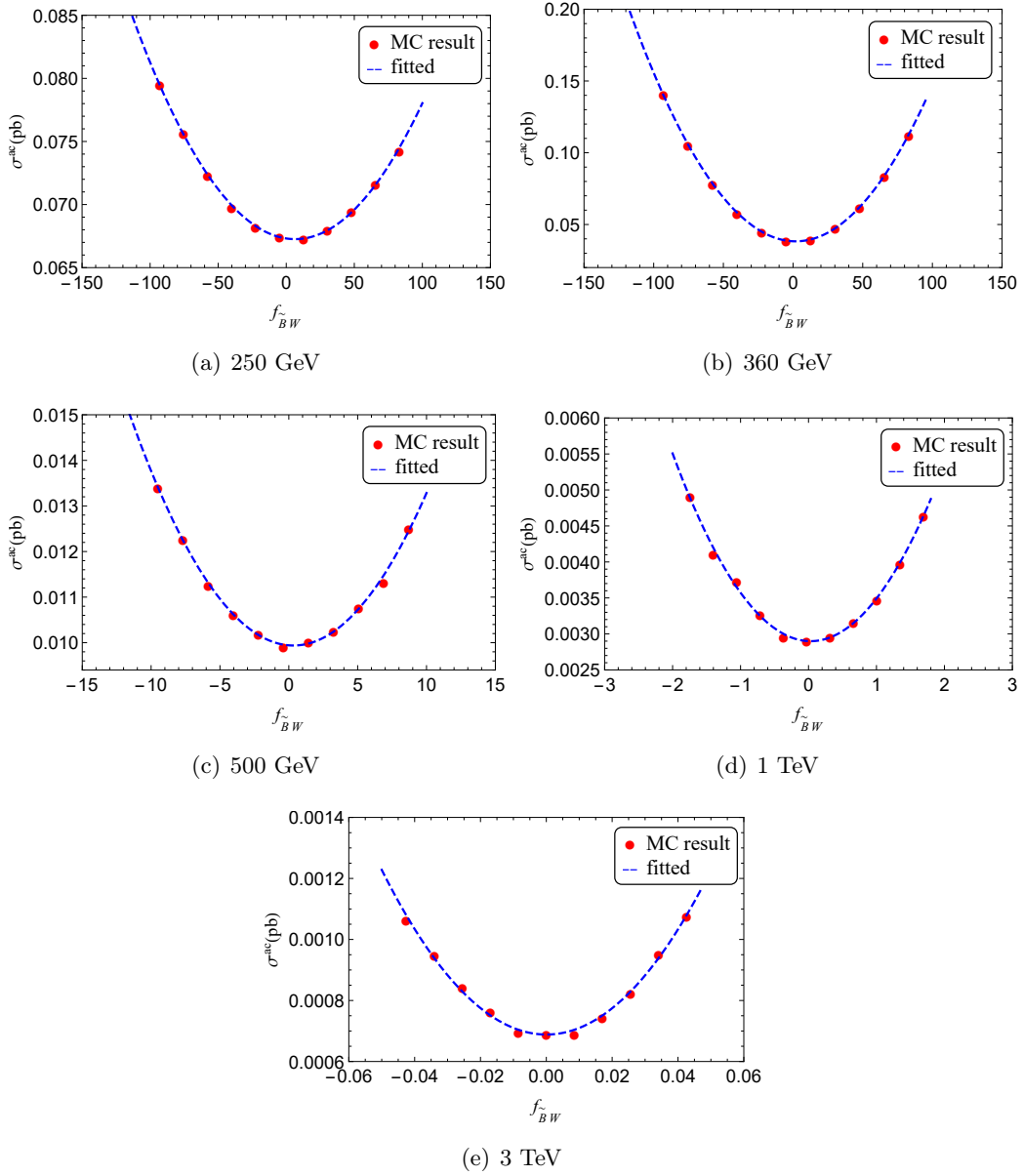


Figure 20: Cross sections as functions of $f_{\tilde{B}W}$ (TeV^{-4}) for $e^+e^- \rightarrow \ell^+\ell^-\nu\bar{\nu}$.

The most significant SM background comes from WW production, where both W bosons decay leptonically. The on-shell ZZ events for this final state can be selected by applying cuts on the invariant mass of the $\ell^+\ell^-$ pair and the missing transverse energy \cancel{E}_T . The missing energy distributions for both the signal and background are similar. Therefore, \cancel{E}_T is not utilized in the event selection strategy. M_{vis} and M_{recoil} are calculated from the reconstructed the Z boson and invisible recoil mass obtained through energy conservation. Then, the normalized sum of visible and recoil masses $(M_{\text{vis}} + M_{\text{recoil}})/\sqrt{s}$ can be used in the analysis. Fig. 19 shows that the distribution of $(M_{\text{vis}} + M_{\text{recoil}})/\sqrt{s}$ exhibits two peaks: one near $2M_Z$, corresponding to ZZ production, and another in a higher mass region, which

is attributed to WW production. Given that the distribution of this observable varies with different collision energies, we propose two distinct sets of cut schemes for CEPC and ILC (CLIC) to enhance selection performance. The specific values of event selection strategy and the respective cut efficiencies are presented in Table 13.

Table 14: The fitted values of $\sigma_{\text{NP}}^{\text{ac}}$ ($\text{fb} \times \text{TeV}^8$) and $\hat{\sigma}_{\text{int}}$ ($\text{fb} \times \text{TeV}^4$) for $e^+e^- \rightarrow \ell^+\ell^-\nu\bar{\nu}$ at each energy point.

\sqrt{s}	250 GeV	360 GeV	500 GeV	1 TeV	3 TeV
$\hat{\sigma}_{\text{int}}$	-0.0161	-0.0429	-0.0241	-0.0403	-0.0132
$\sigma_{\text{NP}}^{\text{ac}}$	0.0012	0.0113	0.0358	0.6316	215.60

With the event selection strategy applied for the final state $\ell^+\ell^-\nu\bar{\nu}$, the cross section fitting functions of $\mathcal{O}_{\tilde{B}W}$ are shown in Fig. 20, and the fitting coefficients of the interference terms are provided in Table 14. The sensitivity analysis and the expected constraints on the $\mathcal{O}_{\tilde{B}W}$ operator are presented in Table 12. Although the $e^+e^- \rightarrow \ell^+\ell^-\nu\bar{\nu}$ channel is not the most optimal, the expected constraints on $f_{\tilde{B}W}$ at 95% confidence level (C.L.) can still reach approximately -4 TeV^{-4} to 8 TeV^{-4} for $\mathcal{O}_{\tilde{B}W}$ at the 360 GeV CEPC. At ILC and CLIC, with higher energy and luminosity, these constraints are further improved, achieving orders of magnitude around 10^{-1} TeV^{-4} and 10^{-2} TeV^{-4} , respectively.

Table 15: The expected constraints on $f_{\tilde{B}W}$ (TeV^{-4}) for $e^+e^- \rightarrow \ell^+\ell^-\nu\bar{\nu}$.

S_{stat}	$\sqrt{s}(\text{GeV})$				
	250	360	500	1000	3000
2	[-8.7, 21.7]	[-4.3, 8.1]	[-2.51, 3.18]	[-0.39, 0.45]	[-0.010, 0.011]
3	[-11.5, 24.6]	[-5.6, 9.4]	[-3.15, 3.83]	[-0.48, 0.55]	[-0.013, 0.013]
5	[-16.2, 29.2]	[-7.7, 11.5]	[-4.19, 4.87]	[-0.64, 0.70]	[-0.017, 0.017]

3.5 Selection of $e^+e^- \rightarrow jj\nu\bar{\nu}$

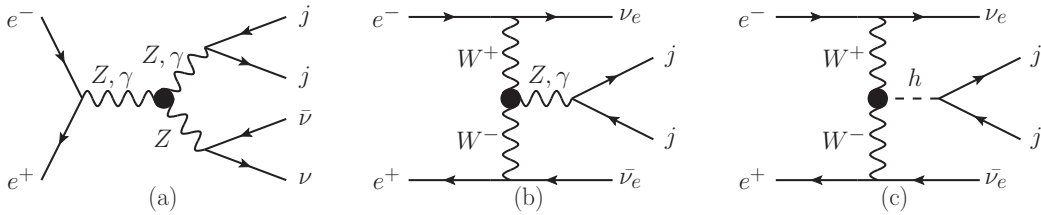


Figure 21: Typical Feynman diagrams which contribute to the process $e^+e^- \rightarrow jj\nu\bar{\nu}$ for signal events.

The signal $jj\nu\bar{\nu}$ from the $\mathcal{O}_{\tilde{B}W}$ operator originates from the diagrams depicted in Fig. 21. In this channel, di-boson production provides the dominant contribution, with the $jj\nu\bar{\nu}$ decay mode representing approximately 28% of the ZZ final states. The key

signature of this decay is a large invisible energy component alongside a pair of jets with a reconstructed mass close to the Z boson mass.

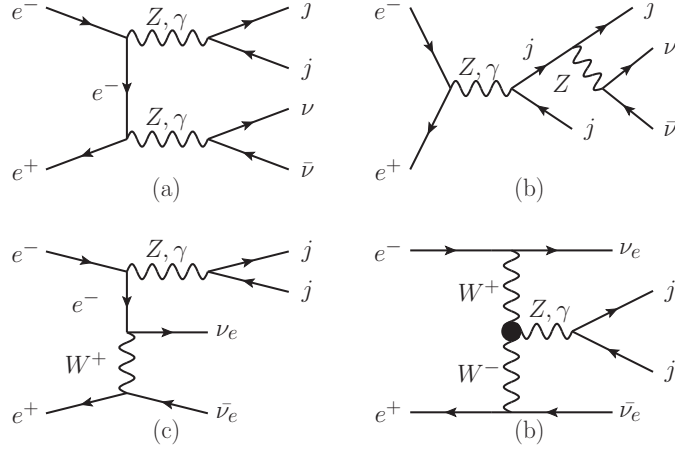


Figure 22: The Feynman diagrams which contribute to the process $e^+e^- \rightarrow jj\nu\bar{\nu}$ for background events.

The most challenging backgrounds arise from multiple sources: di-boson production with one boson undergoing an invisible decay, di-jet events accompanied by energetic vector boson decays, single resonant $Z\nu\bar{\nu}$ production, and the vector boson fusion (VBF) process, as illustrated in Fig. 22.

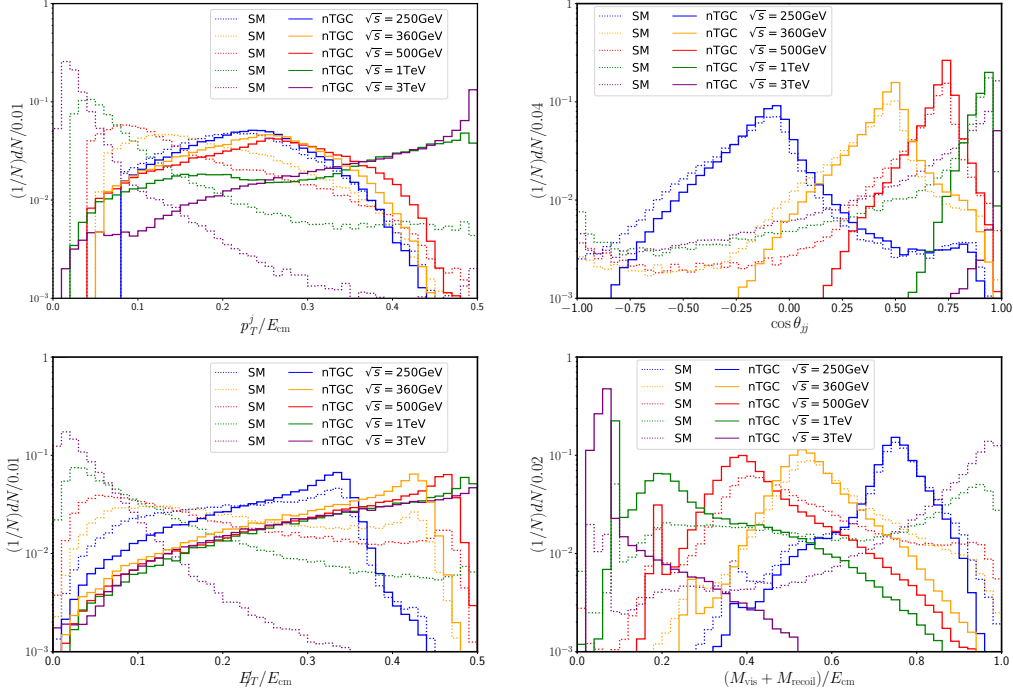


Figure 23: The normalized distributions of p_T^j/E_{cm} , $\cos\theta_{jj}$, E_T/E_{cm} and $(M_{vis} + M_{recoil})/\sqrt{s}$ for $e^+e^- \rightarrow jj\nu\bar{\nu}$

The $\ell^+\ell^-\nu\bar{\nu}$ channel discussed in the previous section exhibit very clean signals at e^+e^- colliders. However, hadronic decay mode hold certain advantages due to their larger branching ratios. For the nTGC signal, events were generated using the largest coefficients listed in Table 3. The kinematic analysis initially selected events containing a hadronic jet with transverse momentum $p_T^j = 10$ GeV and pseudorapidity $|\eta^j| < 2.0$. Following these basic cuts, we required a minimum of two jets in each event, and applied a jet separation criterion of $\Delta R_{jj} = 0.2$, as previously discussed.

The properties of hadronic and invisible decays can effectively differentiate the signal from the SM background. Fig. 23 presents the normalized distributions of p_T^j/E_{cm} , $\cos\theta_{jj}$, $\cancel{E}_T/E_{\text{cm}}$, and $(M_{\text{vis}} + M_{\text{recoil}})/E_{\text{cm}}$. In signal events, the Z or Higgs bosons are generally more energetic than those in background events, leading to a smaller angle between the jets and higher p_T^j values in the signal, predominantly in the high-energy region. The transverse missing energy \cancel{E}_T serves to approximate the transverse energy of the Z boson in its $\nu\bar{\nu}$ decay mode. As expected, \cancel{E}_T in the signal is generally larger than in the background. These distinctions become increasingly pronounced with rising collision energies, particularly at TeV-scale colliders.

Table 16: The event selection strategy and cross sections of $e^+e^- \rightarrow jj\nu\bar{\nu}$ (fb) after cuts.

	$\sqrt{s}=250$ GeV		$\sqrt{s}=360$ GeV			
	SM	NP	SM		NP	
Basic Cuts	198.5	0.614	120.4	8.407		
$\cancel{E}_T/E_{\text{cm}} > 0.1$	173.1	0.574				
$\cancel{E}_T/E_{\text{cm}} > 0.2$			62.61	6.996		
$(M_{\text{vis}} + M_{\text{recoil}}) < 0.9E_{\text{cm}}$	168.6	0.567				
$(M_{\text{vis}} + M_{\text{recoil}}) < 0.8E_{\text{cm}}$			60.92	6.928		
$\cos\theta_{jj} > -0.6$	162.5	0.55				
$\cos\theta_{jj} > -0.2$			59.93	6.894		
Efficiency ϵ	80.3%	89.9%	49%	82%		
	$\sqrt{s}=500$ GeV		$\sqrt{s}=1$ TeV		$\sqrt{s}=3$ TeV	
	SM	NP	SM	NP	SM	NP
Basic Cuts	84.46	0.565	46.12	0.558	44.09	0.385
$\cancel{E}_T/E_{\text{cm}} > 0.3$	21.50	0.379	6.230	0.387	0.805	0.256
$(M_{\text{vis}} + M_{\text{recoil}}) < 0.7E_{\text{cm}}$	21.20	0.377				
$(M_{\text{vis}} + M_{\text{recoil}}) < 0.6E_{\text{cm}}$			5.915	0.381		
$(M_{\text{vis}} + M_{\text{recoil}}) < 0.3E_{\text{cm}}$					0.657	0.249
$\cos\theta_{jj} > 0.2$	20.80	0.375				
$\cos\theta_{jj} > 0.5$			5.787	0.379		
$\cos\theta_{jj} > 0.7$					0.648	0.249
Efficiency ϵ	24%	66%	12%	68%	1.4%	65%

At several hundred GeV, where ZZ production is the main contributor to both signal

and background, the peak of $(M_{\text{vis}} + M_{\text{recoil}})$ primarily appears near $2M_Z$ on the CEPC. As the collision energy increases, the non- ZZ production contributions to the background become more significant, shifting the $(M_{\text{vis}} + M_{\text{recoil}})$ distribution to higher mass regions. This shift improves the background rejection performance of $(M_{\text{vis}} + M_{\text{recoil}})$ at high-energy colliders.

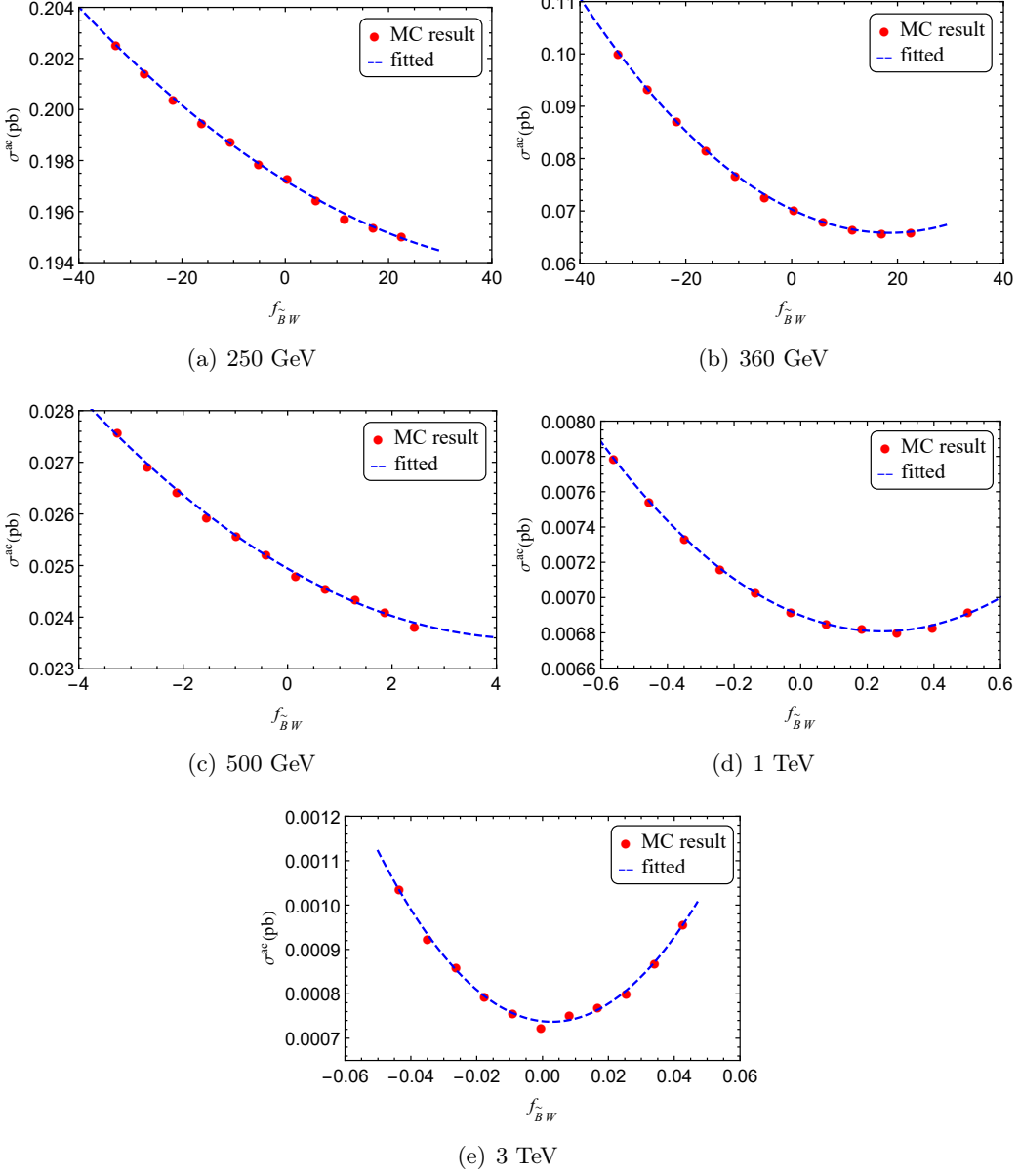


Figure 24: Cross sections as a functions of $f_{\tilde{B}W}$ (TeV^{-4}) for the process $e^+e^- \rightarrow jj\nu\bar{\nu}$ at different c.m. energies.

The specific values of the event selection strategy and corresponding cut efficiencies are presented in Table 16. For the final state $jj\nu\bar{\nu}$, the cross-section fitting functions for $\mathcal{O}_{\tilde{B}W}$

are shown in Fig. 24, and the fitting coefficients for the interference terms are provided in Table 17. The longitudinal polarization contribution of vector bosons dominates the SM background, and this contribution is suppressed by \sqrt{s} due to an exact cancellation with the VBS process. In contrast, the cross section of the signal induced by nTGC increases with rising \sqrt{s} . The energy-dependent interference term depends on the combined effect of this enhancement and depression. Consequently, as shown in Fig. 24, the interference between the nTGC signal and the SM background for the process $e^+e^- \rightarrow jj\nu\bar{\nu}$ decreases with increasing energy. Table 18 presents the expected constraints on the nTGC operators, obtained by fitting the observed $jj\nu\bar{\nu}$ events for 2σ , 3σ , and 5σ significance levels at future e^+e^- colliders.

Table 17: The fitted values of $\sigma_{\text{NP}}^{\text{ac}}$ ($\text{fb} \times \text{TeV}^8$) and $\hat{\sigma}_{\text{int}}$ ($\text{fb} \times \text{TeV}^4$) for $e^+e^- \rightarrow jj\nu\bar{\nu}$ at each energy point.

\sqrt{s}	250 GeV	360 GeV	500 GeV	1 TeV	3 TeV
$\hat{\sigma}_{\text{int}}$	-0.1252	-0.4851	-0.6432	-0.7372	-0.7797
$\sigma_{\text{NP}}^{\text{ac}}$	0.0011	0.0131	0.0660	1.5071	137.88

Summarizing the expected constraints obtained for the five channels in this section, the $4j$ signal provides the strongest constraint among the five possible nTGC signals produced by the $e^+e^- \rightarrow ZZ$ process. Potential improvements in these constraints through combined analyses are discussed in section 3.6.

Table 18: The expected constraints on $f_{\tilde{B}W}$ (TeV^{-4}) for $e^+e^- \rightarrow jj\nu\bar{\nu}$.

S_{stat}	\sqrt{s} (GeV)				
	250	360	500	1000	3000
2	[-3.1, 114.5]	[-1.1, 38.0]	[-0.7, 10.0]	[-0.17, 0.66]	[-0.011, 0.017]
3	[-4.6, 116.0]	[-1.6, 38.5]	[-1.0, 10.3]	[-0.23, 0.72]	[-0.014, 0.020]
5	[-7.5, 118.9]	[-2.6, 39.5]	[-1.7, 10.9]	[-0.34, 0.83]	[-0.019, 0.024]

3.6 Constraints on the coefficients with combined results

By combining the results obtained from the five decay modes analyzed in this section, it is possible to extract more competitive constraints beyond those provided by the each decay mode alone. Based on the formula

$$\mathcal{S}_{\text{stat}}^{\text{comb}} = \sqrt{\sum S_{\text{stat}}^2(i)}, \quad (3.9)$$

where $S_{\text{stat}}(i)$ is signal significance function for each decay mode of ZZ production. The numerical results of expected coefficient constraints, combining data from the five decay patterns, are presented in Table 19. These constraints provide insight into the behavior of the coefficients for the $\mathcal{O}_{\tilde{B}W}$ operator across different \sqrt{s} ranging from 250 GeV to 3 TeV.

We further made comparisons between the LHC constraints on $\mathcal{O}_{\tilde{B}W}$ at $\sqrt{s} = 13$ TeV [73] and our predictions. The Observed 95% CL limits on the $f_{\tilde{B}W}$ is $(-1.1, 1.1)$ via

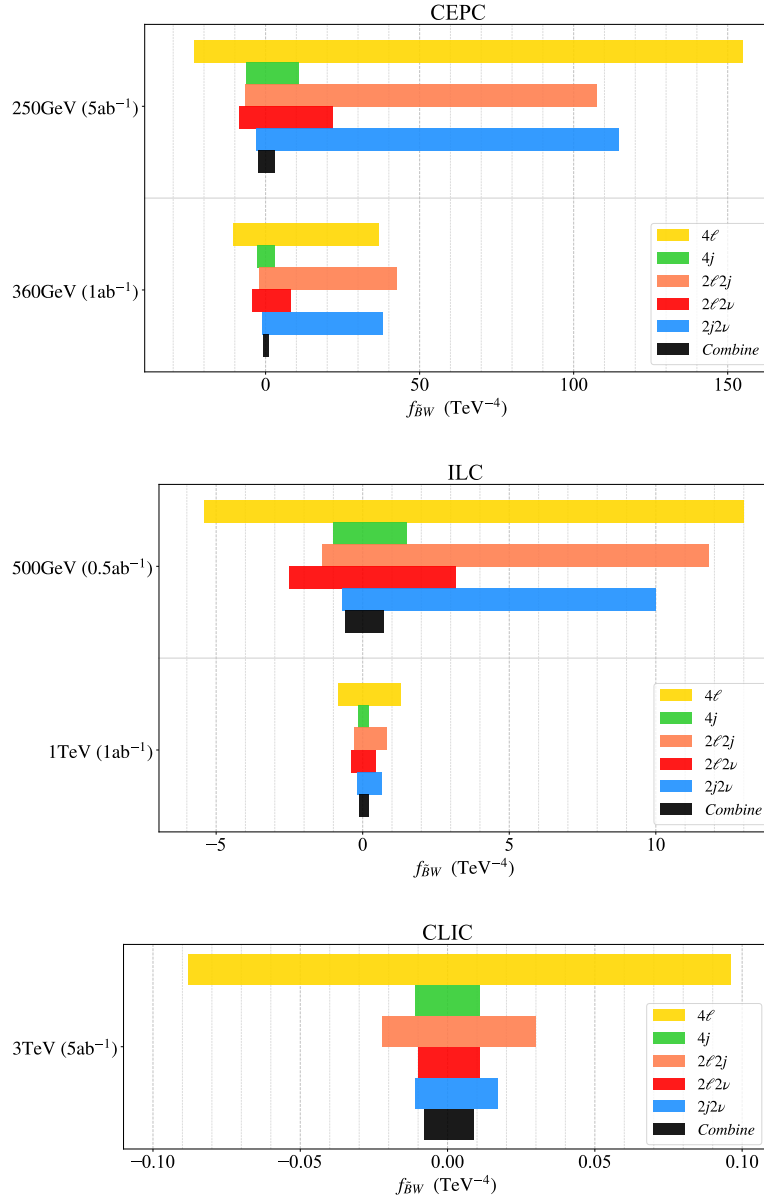


Figure 25: Constraints on $f_{\tilde{B}W}$ (TeV⁻⁴) for different colliders with combined results at 95% CL level.

measurement of the $Z\gamma \rightarrow \nu\bar{\nu}\gamma$ production. We found that with an appropriate event selection strategy, the $e^+e^- \rightarrow ZZ$ process signal with decays at the 250 GeV CEPC is slightly less sensitive to nTGCs compared to measurements at the LHC. However, as the CEPC collision energy increases to 360 GeV, its detection capability for nTGCs is anticipated to surpass that of the LHC. The expected constraints on nTGCs by the ILC of $\sqrt{s} = 1$ TeV with $\mathcal{L} = 1$ ab⁻¹ can be improved by an order of magnitude over the LHC of 13 TeV; and that for the CLIC with $\sqrt{s} = 3$ TeV and $\mathcal{L} = 5$ ab⁻¹, the expected constraints

at $\mathcal{S}_{stat} = 2$ are about two orders of magnitude stronger than those at the $\sqrt{s} = 13$ TeV LHC at 95% C.L. We anticipate that machine learning techniques can further enhance the sensitivity of nTGC measurements.

Table 19: The combined constraints on $f_{\tilde{B}W}$ (TeV^{-4}) for five signal channels of ZZ production.

\mathcal{S}_{stat}	\sqrt{s} (GeV)				
	250	360	500	1000	3000
2	[-2.43, 2.64]	[-0.90, 0.96]	[-0.52, 0.61]	[-0.14, 0.36]	[-0.0079, 0.0093]
3	[-3.57, 4.02]	[-1.31, 1.42]	[-0.75, 0.92]	[-0.19, 0.47]	[-0.0099, 0.0112]
5	[-5.69, 6.88]	[-2.05, 2.28]	[-1.14, 1.49]	[-0.28, 0.59]	[-0.0131, 0.0145]

4 Conclusions

Precision measurements of the self-couplings of electroweak gauge bosons are essential for testing the EWSB mechanism and for probing potential NP beyond the SM. nTGCs represent a possible class of anomalous multi-boson couplings within the framework of the SMEFT. Unlike the more commonly studied dimension-6 TGCs in SMEFT, nTGCs arise first from gauge-invariant dimension-8 operators. nTGCs can contribute to the process $e^+e^- \rightarrow ZZ$ through the ZZZ and $ZZ\gamma$ vertices. The potential contributions of nTGCs to this process can be investigated at future e^+e^- colliders, such as CEPC, ILC and CLIC. In this paper, we have demonstrated that these future e^+e^- colliders possess the capability to measure nTGCs through ZZ pair production.

We first study the influence of initial beam polarization on the measurement of $e^+e^- \rightarrow ZZ$. Specific polarization settings can enhance the cross section at an e^+e^- collider. For instance, the cross section $\sigma_{+-,+}$ of nTGCs can be twice that of the unpolarized cross section. In the case of SM contributions, the polarized cross sections σ_{-+} and σ_{+-} are approximately 2.5 and 1.5 times larger, respectively, than the unpolarized cross section. Consequently, we adopt an electron polarization of +0.8 and a positron polarization of -0.8 in our simulations and analyses for future e^+e^- colliders.

Additionally, we present a kinematic analysis of the sensitivity of measurements of five distinct final states of ZZ production induced by nTGCs at future e^+e^- colliders. To this end, we study the kinematic features of the signal and background events using Monte Carlo simulations, and propose an event selection strategy for nTGCs. The expected constraints on the coefficients of dimension-8 operators are calculated by combining results from future e^+e^- colliders with c.m. energies of 250 GeV, 360 GeV, 500 GeV, 1 TeV and 3 TeV, characteristic of CEPC, ILC, and CLIC. As expected, higher collision energies lead to greater sensitivities. The greatest sensitivity to ZZ production is generally provided by the $ZZ \rightarrow jj\nu\bar{\nu}$ decay channel, while combining results from multiple channels further enhances the sensitivity to nTGC operators.

We also performed quantitative comparisons between the existing limits on $\mathcal{O}_{\tilde{B}W}$ from the 13 TeV LHC and our predictions. The results indicate that the sensitivity of CEPC in

detecting nTGCs is comparable to that of the LHC. Furthermore, when the collision energy increases from 250 GeV to 360 GeV, the detection capability of CEPC for nTGCs improves by approximately threefold. On the other hand, higher-energy e^+e^- colliders ($\sqrt{s} = 1 \sim 3$ TeV) are expected to achieve greater sensitivities than the LHC. Measurements of nTGCs at the ILC and CLIC have the potential to improve current constraints on dimension-8 operators by one to two orders of magnitude. These findings further illustrate the potential for exploring and constraining dimension-8 operators within the SMEFT, complementing existing searches for aQGCs [20–25, 38–41] and gQGCs [27] discussed elsewhere.

Acknowledgments

This work was supported in part by the National Natural Science Foundation of China under Grants Nos. 11905093 and 12147214, the Natural Science Foundation of the Liaoning Scientific Committee No. JYTMS20231053 and LJKZ0978.

A Helicity amplitudes

The helicity amplitudes for the $e^+e^- \rightarrow ZZ$ process are given below. Here, θ and ϕ represent the zenith and azimuthal angles of one of the Z bosons, defined in the rest frame of the e^+e^- system, where the electron is moving along the z -axis.

$$\mathcal{A} = \frac{1}{\sqrt{2}c_W^2 s_W^2 \left(s(4M_Z^2 - s) \cos^2(\theta) + (s - 2M_Z^2)^2 \right)}, \quad (\text{A.1})$$

$$\mathcal{M}_{+,+,0,0} = 16\sqrt{2}\mathcal{A}\pi\alpha_{EW} s M_Z^2 e^{i\phi} s_W^4 \sin(2\theta), \quad (\text{A.2})$$

$$\begin{aligned} \mathcal{M}_{+,+,0,\pm} = \mp \mathcal{A} M_Z e^{i\phi} \sqrt{s} s_W^2 (\cos(\theta) \pm 1) & \left(\mp s_W (2M_Z^2 - s) (\pm c_W^3 f_{\bar{B}W} (8M_Z^4 - 6M_Z^2 s + s^2) \right. \\ & \left. + 16\pi\alpha_{EW} s_W) + s_W \cos(\theta) s \left(c_W^3 f_{\bar{B}W} (s - 4M_Z^2)^2 \cos(\theta) + 16\pi\alpha_{EW} s_W \right) \right), \end{aligned} \quad (\text{A.3})$$

$$\begin{aligned} \mathcal{M}_{+,+, \pm, 0} = \mathcal{A} M_Z e^{i\phi} \sqrt{s} s_W^2 (\cos(\theta) \mp 1) & \left(s_W (2M_Z^2 - s) (c_W^3 f_{\bar{B}W} (8M_Z^4 - 6M_Z^2 s + s^2) \right. \\ & \left. + 16\pi\alpha_{EW}^2 s_W) + s_W \cos(\theta) s \left(c_W^3 f_{\bar{B}W} (s - 4M_Z^2)^2 \cos(\theta) \mp 16\pi\alpha_{EW}^2 s_W \right) \right), \end{aligned} \quad (\text{A.4})$$

$$\mathcal{M}_{+,+, \pm, \pm} = -8\sqrt{2}\mathcal{A}\pi\alpha_{EW}^2 s M_Z^2 e^{i\phi} s_W^4 \sin(2\theta), \quad (\text{A.5})$$

$$\mathcal{M}_{+,+, +, -} = -16\sqrt{2}\mathcal{A}\pi\alpha_{EW}^2 s e^{i\phi} s_W^4 (s - 2M_Z^2) \sin^2\left(\frac{\theta}{2}\right) \sin(\theta), \quad (\text{A.6})$$

$$\mathcal{M}_{+,+, -, +} = 4\sqrt{2}\mathcal{A}\pi\alpha_{EW}^2 s e^{i\phi} s_W^4 (s - 2M_Z^2) \sin^3(\theta) \csc^2\left(\frac{\theta}{2}\right), \quad (\text{A.7})$$

$$\mathcal{M}_{-, -, 0, 0} = -4\sqrt{2}\mathcal{A} (1 - 2c_W^2)^2 \pi\alpha_{EW}^2 s M_Z^2 e^{-i\phi} \sin(2\theta), \quad (\text{A.8})$$

$$\begin{aligned} \mathcal{M}_{-,-,0,\pm} = & \mathcal{A}M_Z e^{-i\phi} \sqrt{s} (\cos(\theta) \mp 1) \left((2M_Z^2 - s) \left(- (1 - 2c_W^2)^2 4\pi\alpha_{EW}^2 \right. \right. \\ & \left. \left. + c_W^3 f_{\tilde{B}W} s_W^3 (8M_Z^4 - 6M_Z^2 s + s^2) \right) + s \cos(\theta) \left(\pm (1 - 2c_W^2)^2 4\pi\alpha_{EW}^2 \right. \right. \\ & \left. \left. + c_W^3 f_{\tilde{B}W} s_W^3 (s - 4M_Z^2)^2 \cos(\theta) \right) \right), \end{aligned} \quad (\text{A.9})$$

$$\begin{aligned} \mathcal{M}_{-,-,\pm,0} = & \pm \mathcal{A}M_Z e^{-i\phi} \sqrt{s} (\cos(\theta) \pm 1) \left((2M_Z^2 - s) \left(\pm (1 - 2c_W^2)^2 4\pi\alpha_{EW}^2 \right. \right. \\ & \left. \left. \mp c_W^3 f_{\tilde{B}W} s_W^3 (8M_Z^4 - 6M_Z^2 s + s^2) \right) + s \cos(\theta) \left((1 - 2c_W^2)^2 4\pi\alpha_{EW}^2 \right. \right. \\ & \left. \left. \mp c_W^3 f_{\tilde{B}W} s_W^3 (s - 4M_Z^2)^2 \cos(\theta) \right) \right), \end{aligned} \quad (\text{A.10})$$

$$\mathcal{M}_{-,-,\pm,\pm} = 4\sqrt{2}\mathcal{A} (1 - 2c_W^2)^2 \pi\alpha_{EW}^2 s M_Z^2 e^{-i\phi} \sin(\theta) \cos(\theta), \quad (\text{A.11})$$

$$\mathcal{M}_{-,-,+,-} = -2\sqrt{2}\mathcal{A} e^{-i\phi} s (4\pi\alpha_{EW} - 8c_W^2 \pi\alpha_{EW})^2 (s - 2M_Z^2) \sin\left(\frac{\theta}{2}\right) \cos^3\left(\frac{\theta}{2}\right), \quad (\text{A.12})$$

$$\mathcal{M}_{-,-,-,+} = 4\sqrt{2}\mathcal{A} (1 - 2c_W^2)^2 \pi\alpha_{EW}^2 e^{-i\phi} s (s - 2M_Z^2) \sin^2\left(\frac{\theta}{2}\right) \sin(\theta). \quad (\text{A.13})$$

References

- [1] S. Weinberg, *Baryon and Lepton Nonconserving Processes*, *Phys. Rev. Lett.* **43** (1979) 1566.
- [2] B. Grzadkowski, M. Iskrzynski, M. Misiak and J. Rosiek, *Dimension-Six Terms in the Standard Model Lagrangian*, *JHEP* **10** (2010) 085 [[1008.4884](#)].
- [3] S. Willenbrock and C. Zhang, *Effective Field Theory Beyond the Standard Model*, *Ann. Rev. Nucl. Part. Sci.* **64** (2014) 83 [[1401.0470](#)].
- [4] E. Masso, *An Effective Guide to Beyond the Standard Model Physics*, *JHEP* **10** (2014) 128 [[1406.6376](#)].
- [5] S. Willenbrock and C. Zhang, *Effective Field Theory Beyond the Standard Model*, *Ann. Rev. Nucl. Part. Sci.* **64** (2014) 83 [[1401.0470](#)].
- [6] G. J. Gounaris, J. Layssac and F. M. Renard, *Off-shell structure of the anomalous Z and γ selfcouplings*, *Phys. Rev. D* **62** (2000) 073012 [[hep-ph/0005269](#)].
- [7] A. Senol, H. Denizli, A. Yilmaz, I. Turk Cakir, K. Y. Oyulmaz, O. Karadeniz et al., *Probing the Effects of Dimension-eight Operators Describing Anomalous Neutral Triple Gauge Boson Interactions at FCC-hh*, *Nucl. Phys. B* **935** (2018) 365 [[1805.03475](#)].
- [8] G. J. Gounaris, J. Layssac and F. M. Renard, *Signatures of the anomalous $Z\gamma$ and ZZ production at the lepton and hadron colliders*, *Phys. Rev. D* **61** (2000) 073013 [[hep-ph/9910395](#)].
- [9] C. Degrande, *A basis of dimension-eight operators for anomalous neutral triple gauge boson interactions*, *JHEP* **02** (2014) 101 [[1308.6323](#)].
- [10] J. Ellis and S.-F. Ge, *Constraining Gluonic Quartic Gauge Coupling Operators with $gg \rightarrow \gamma\gamma$* , *Phys. Rev. Lett.* **121** (2018) 041801 [[1802.02416](#)].
- [11] C. Zhang and S.-Y. Zhou, *Positivity bounds on vector boson scattering at the LHC*, *Phys. Rev. D* **100** (2019) 095003 [[1808.00010](#)].

- [12] B. Henning, X. Lu, T. Melia and H. Murayama, *2, 84, 30, 993, 560, 15456, 11962, 261485, ...: Higher dimension operators in the SM EFT*, *JHEP* **08** (2017) 016 [[1512.03433](#)].
- [13] C. Arzt, M. Einhorn and J. Wudka, *Patterns of deviation from the standard model*, *Nucl. Phys. B* **433** (1995) 41 [[hep-ph/9405214](#)].
- [14] G. Perez, M. Sekulla and D. Zeppenfeld, *Anomalous quartic gauge couplings and unitarization for the vector boson scattering process $pp \rightarrow W^+W^+jjX \rightarrow \ell^+\nu_\ell\ell^+\nu_\ell jjX$* , *Eur. Phys. J. C* **78** (2018) 759 [[1807.02707](#)].
- [15] O. Eboli, M. Gonzalez-Garcia and J. Mizukoshi, *$pp \rightarrow jje^\pm\mu^\pm\nu\nu$ and $jje^\pm\mu^\mp\nu\nu$ at $\mathcal{O}(\alpha_\pm^6)$ and $\mathcal{O}(\alpha_\pm^4\alpha_s^2)$ for the study of the quartic electroweak gauge boson vertex at CERN LHC*, *Phys. Rev. D* **74** (2006) 073005 [[hep-ph/0606118](#)].
- [16] O. J. P. Éboli and M. C. Gonzalez-Garcia, *Classifying the bosonic quartic couplings*, *Phys. Rev. D* **93** (2016) 093013 [[1604.03555](#)].
- [17] Q. Bi, C. Zhang and S.-Y. Zhou, *Positivity constraints on aQGC: carving out the physical parameter space*, *JHEP* **06** (2019) 137 [[1902.08977](#)].
- [18] C. Zhang and S.-Y. Zhou, *Convex Geometry Perspective to the (Standard Model) Effective Field Theory Space*, *Phys. Rev. Lett.* **125** (2020) 201601 [[2005.03047](#)].
- [19] J. Ellis, N. E. Mavromatos and T. You, *Light-by-Light Scattering Constraint on Born-Infeld Theory*, *Phys. Rev. Lett.* **118** (2017) 261802 [[1703.08450](#)].
- [20] Y.-C. Guo, Y.-Y. Wang and J.-C. Yang, *Constraints on anomalous quartic gauge couplings by $\gamma\gamma \rightarrow W^+W^-$ scattering*, *Nucl. Phys. B* **961** (2020) 115222 [[1912.10686](#)].
- [21] Y.-C. Guo, Y.-Y. Wang, J.-C. Yang and C.-X. Yue, *Constraints on anomalous quartic gauge couplings via $W\gamma jj$ production at the LHC*, *Chin. Phys. C* **44** (2020) 123105 [[2002.03326](#)].
- [22] L. Jiang, Y.-C. Guo and J.-C. Yang, *Detecting anomalous quartic gauge couplings using the isolation forest machine learning algorithm*, *Phys. Rev. D* **104** (2021) 035021 [[2103.03151](#)].
- [23] J.-C. Yang, Y.-C. Guo, C.-X. Yue and Q. Fu, *Constraints on anomalous quartic gauge couplings via $Z\gamma jj$ production at the LHC*, *Phys. Rev. D* **104** (2021) 035015 [[2107.01123](#)].
- [24] J.-C. Yang, J.-H. Chen and Y.-C. Guo, *Extract the energy scale of anomalous $\gamma\gamma \rightarrow W^+W^-$ scattering in the vector boson scattering process using artificial neural networks*, *JHEP* **09** (2021) 085 [[2107.13624](#)].
- [25] J.-C. Yang, X.-Y. Han, Z.-B. Qin, T. Li and Y.-C. Guo, *Measuring the anomalous quartic gauge couplings in the $W^+W^- \rightarrow W^+W^-$ process at muon collider using artificial neural networks*, *JHEP* **09** (2022) 074 [[2204.10034](#)].
- [26] V. Ari, E. Gurkanli, M. Köksal, A. Gutiérrez-Rodríguez and M. A. Hernández-Ruiz, *Study of the projected sensitivity on the anomalous quartic gauge couplings via $Z\gamma\gamma$ production at the CLIC*, *Nucl. Phys. B* **989** (2023) 116133 [[2112.03948](#)].
- [27] J.-C. Yang, Y.-C. Guo and Y.-F. Dong, *Study of the gluonic quartic gauge couplings at muon colliders*, *Commun. Theor. Phys.* **75** (2023) 115201 [[2307.04207](#)].
- [28] Y.-T. Zhang, X.-T. Wang and J.-C. Yang, *Searching for gluon quartic gauge couplings at muon colliders using the autoencoder*, *Phys. Rev. D* **109** (2024) 095028 [[2311.16627](#)].
- [29] J. Ellis and S.-F. Ge, *Constraining Gluonic Quartic Gauge Coupling Operators with $gg \rightarrow \gamma\gamma$* , *Phys. Rev. Lett.* **121** (2018) 041801 [[1802.02416](#)].

- [30] J. Ellis, S.-F. Ge and K. Ma, *Hadron collider probes of the quartic couplings of gluons to the photon and Z boson*, *JHEP* **04** (2022) 123 [2112.06729].
- [31] J. Ellis, S.-F. Ge, H.-J. He and R.-Q. Xiao, *Probing the scale of new physics in the $ZZ\gamma$ coupling at e^+e^- colliders*, *Chin. Phys. C* **44** (2020) 063106 [1902.06631].
- [32] J. Ellis, H.-J. He and R.-Q. Xiao, *Probing new physics in dimension-8 neutral gauge couplings at e^+e^- colliders*, *Sci. China Phys. Mech. Astron.* **64** (2021) 221062 [2008.04298].
- [33] J. Ellis, H.-J. He and R.-Q. Xiao, *Probing neutral triple gauge couplings at the LHC and future hadron colliders*, *Phys. Rev. D* **107** (2023) 035005 [2206.11676].
- [34] J. Ellis, H.-J. He and R.-Q. Xiao, *Probing neutral triple gauge couplings with $Z^*\gamma(\nu\bar{\nu}\gamma)$ production at hadron colliders*, *Phys. Rev. D* **108** (2023) L111704 [2308.16887].
- [35] D. Liu, R.-Q. Xiao, S. Li, J. Ellis, H.-J. He and R. Yuan, *Probing Neutral Triple Gauge Couplings via $Z\gamma(\ell^+\ell^-\gamma)$ Production at e^+e^- Colliders*, **2404.15937**.
- [36] Q. Fu, J.-C. Yang, C.-X. Yue and Y.-C. Guo, *The study of neutral triple gauge couplings in the process $e^+e^- \rightarrow Z\gamma$ including unitarity bounds*, *Nucl. Phys. B* **972** (2021) 115543 [2102.03623].
- [37] J.-C. Yang, Y.-C. Guo and L.-H. Cai, *Using a nested anomaly detection machine learning algorithm to study the neutral triple gauge couplings at an $e+e-$ collider*, *Nucl. Phys. B* **977** (2022) 115735 [2111.10543].
- [38] J.-C. Yang, Z.-B. Qing, X.-Y. Han, Y.-C. Guo and T. Li, *Tri-photon at muon collider: a new process to probe the anomalous quartic gauge couplings*, *JHEP* **22** (2020) 053 [2204.08195].
- [39] Y.-F. Dong, Y.-C. Mao and J.-C. Yang, *Searching for anomalous quartic gauge couplings at muon colliders using principal component analysis*, *Eur. Phys. J. C* **83** (2023) 555 [2304.01505].
- [40] S. Zhang, J.-C. Yang and Y.-C. Guo, *Using k-means assistant event selection strategy to study anomalous quartic gauge couplings at muon colliders*, *Eur. Phys. J. C* **84** (2024) 142 [2302.01274].
- [41] S. Zhang, Y.-C. Guo and J.-C. Yang, *Optimize the event selection strategy to study the anomalous quartic gauge couplings at muon colliders using the support vector machine and quantum support vector machine*, **2311.15280**.
- [42] ATLAS collaboration, *Evidence for Electroweak Production of $W^\pm W^\pm jj$ in pp Collisions at $\sqrt{s} = 8$ TeV with the ATLAS Detector*, *Phys. Rev. Lett.* **113** (2014) 141803 [1405.6241].
- [43] CMS collaboration, *Measurements of production cross sections of WZ and same-sign WW boson pairs in association with two jets in proton-proton collisions at $\sqrt{s} = 13$ TeV*, *Phys. Lett. B* **809** (2020) 135710 [2005.01173].
- [44] ATLAS collaboration, *Studies of $Z\gamma$ production in association with a high-mass dijet system in pp collisions at $\sqrt{s} = 8$ TeV with the ATLAS detector*, *JHEP* **07** (2017) 107 [1705.01966].
- [45] CMS collaboration, *Measurement of the cross section for electroweak production of $Z\gamma$ in association with two jets and constraints on anomalous quartic gauge couplings in proton-proton collisions at $\sqrt{s} = 8$ TeV*, *Phys. Lett. B* **770** (2017) 380 [1702.03025].
- [46] CMS collaboration, *Measurement of the cross section for electroweak production of a Z boson, a photon and two jets in proton-proton collisions at $\sqrt{s} = 13$ TeV and constraints on anomalous quartic couplings*, *JHEP* **06** (2020) 076 [2002.09902].

- [47] CMS collaboration, *Measurement of electroweak-induced production of $W\gamma$ with two jets in pp collisions at $\sqrt{s} = 8$ TeV and constraints on anomalous quartic gauge couplings*, *JHEP* **06** (2017) 106 [[1612.09256](#)].
- [48] CMS collaboration, *Measurement of vector boson scattering and constraints on anomalous quartic couplings from events with four leptons and two jets in proton–proton collisions at $\sqrt{s} = 13$ TeV*, *Phys. Lett. B* **774** (2017) 682 [[1708.02812](#)].
- [49] CMS collaboration, *Measurement of differential cross sections for Z boson pair production in association with jets at $\sqrt{s} = 8$ and 13 TeV*, *Phys. Lett. B* **789** (2019) 19 [[1806.11073](#)].
- [50] ATLAS collaboration, *Observation of electroweak $W^\pm Z$ boson pair production in association with two jets in pp collisions at $\sqrt{s} = 13$ TeV with the ATLAS detector*, *Phys. Lett. B* **793** (2019) 469 [[1812.09740](#)].
- [51] CMS collaboration, *Measurement of electroweak WZ boson production and search for new physics in $WZ +$ two jets events in pp collisions at $\sqrt{s} = 13$ TeV*, *Phys. Lett. B* **795** (2019) 281 [[1901.04060](#)].
- [52] CMS collaboration, *Evidence for exclusive $\gamma\gamma \rightarrow W^+W^-$ production and constraints on anomalous quartic gauge couplings in pp collisions at $\sqrt{s} = 7$ and 8 TeV*, *JHEP* **08** (2016) 119 [[1604.04464](#)].
- [53] CMS collaboration, *Observation of electroweak production of same-sign W boson pairs in the two jet and two same-sign lepton final state in proton-proton collisions at $\sqrt{s} = 13$ TeV*, *Phys. Rev. Lett.* **120** (2018) 081801 [[1709.05822](#)].
- [54] CMS collaboration, *Search for anomalous electroweak production of vector boson pairs in association with two jets in proton-proton collisions at 13 TeV*, *Phys. Lett. B* **798** (2019) 134985 [[1905.07445](#)].
- [55] CMS collaboration, *Observation of electroweak production of $W\gamma$ with two jets in proton-proton collisions at $\sqrt{s} = 13$ TeV*, *Phys. Lett. B* **811** (2020) 135988 [[2008.10521](#)].
- [56] CMS collaboration, *Evidence for electroweak production of four charged leptons and two jets in proton-proton collisions at $\sqrt{s} = 13$ TeV*, *Phys. Lett. B* **812** (2021) 135992 [[2008.07013](#)].
- [57] G. J. Gounaris, J. Layssac and F. M. Renard, *New and standard physics contributions to anomalous Z and gamma selfcouplings*, *Phys. Rev. D* **62** (2000) 073013 [[hep-ph/0003143](#)].
- [58] D. Choudhury, S. Dutta, S. Rakshit and S. Rindani, *Trilinear neutral gauge boson couplings*, *Int. J. Mod. Phys. A* **16** (2001) 4891 [[hep-ph/0011205](#)].
- [59] C.-X. Yue, X.-J. Cheng and J.-C. Yang, *Charged-current non-standard neutrino interactions at the LHC and HL-LHC**, *Chin. Phys. C* **47** (2023) 043111 [[2110.01204](#)].
- [60] S. Dutta, A. Goyal and Mamta, *New Physics Contribution to Neutral Trilinear Gauge Boson Couplings*, *Eur. Phys. J. C* **63** (2009) 305 [[0901.0260](#)].
- [61] N. G. Deshpande and X.-G. He, *Triple neutral gauge boson couplings in noncommutative standard model*, *Phys. Lett. B* **533** (2002) 116 [[hep-ph/0112320](#)].
- [62] N. G. Deshpande and S. K. Garg, *Anomalous triple gauge boson couplings in $e^-e^+ \rightarrow \gamma\gamma$ for noncommutative standard model*, *Phys. Lett. B* **708** (2012) 150 [[1111.5173](#)].
- [63] D. Chang, W.-Y. Keung and P. B. Pal, *CP violation in the cubic coupling of neutral gauge bosons*, *Phys. Rev. D* **51** (1995) 1326 [[hep-ph/9407294](#)].

- [64] J.-C. Yang and M.-Z. Yang, *Effect of the Charged Higgs Bosons in the Radiative Leptonic Decays of B^- and D^- Mesons*, *Mod. Phys. Lett. A* **31** (2015) 1650012 [[1508.00314](#)].
- [65] K. Agashe and N. G. Deshpande, *Limits on low scale gravity from $e^+ e^- \rightarrow W^+ W^-$, $Z Z$ and gamma gamma*, *Phys. Lett. B* **456** (1999) 60 [[hep-ph/9902263](#)].
- [66] B. Ananthanarayan, S. K. Garg, M. Patra and S. D. Rindani, *Isolating CP-violating γZZ coupling in $e^+ e^- \rightarrow \gamma Z$ with transverse beam polarizations*, *Phys. Rev. D* **85** (2012) 034006 [[1104.3645](#)].
- [67] B. Ananthanarayan, J. Lahiri, M. Patra and S. D. Rindani, *New physics in $e^+ e^- \rightarrow Z\gamma$ at the ILC with polarized beams: explorations beyond conventional anomalous triple gauge boson couplings*, *JHEP* **08** (2014) 124 [[1404.4845](#)].
- [68] S. Spor, E. Gurkanli and M. Köksal, *Search for the anomalous $ZZ\gamma$ and $Z\gamma\gamma$ couplings via $\nu\nu\gamma$ production at the CLIC*, *Nucl. Phys. B* **979** (2022) 115785 [[2203.02352](#)].
- [69] A. Senol, H. Denizli, A. Yilmaz, I. Turk Cakir, K. Oyulmaz, O. Karadeniz et al., *Probing the effects of dimension-eight operators describing anomalous neutral triple gauge boson interactions at fcc-hh*, *Nuclear Physics B* **935** (2018) 365.
- [70] CEPC PHYSICS STUDY GROUP collaboration, *The Physics potential of the CEPC. Prepared for the US Snowmass Community Planning Exercise (Snowmass 2021)*, in *Snowmass 2021*, 5, 2022, [2205.08553](#).
- [71] ILC INTERNATIONAL DEVELOPMENT TEAM collaboration, *The International Linear Collider: Report to Snowmass 2021*, [2203.07622](#).
- [72] R. Franceschini et al., *The CLIC Potential for New Physics*, [1812.02093](#).
- [73] ATLAS collaboration, *Measurement of the $Z\gamma \rightarrow \nu\bar{\nu}\gamma$ production cross section in pp collisions at $\sqrt{s} = 13$ TeV with the ATLAS detector and limits on anomalous triple gauge-boson couplings*, *JHEP* **12** (2018) 010 [[1810.04995](#)].
- [74] J. Alwall, R. Frederix, S. Frixione, V. Hirschi, F. Maltoni, O. Mattelaer et al., *The automated computation of tree-level and next-to-leading order differential cross sections, and their matching to parton shower simulations*, *JHEP* **07** (2014) 079 [[1405.0301](#)].
- [75] N. D. Christensen and C. Duhr, *FeynRules - Feynman rules made easy*, *Comput. Phys. Commun.* **180** (2009) 1614 [[0806.4194](#)].
- [76] T. Sjöstrand, S. Ask, J. R. Christiansen, R. Corke, N. Desai, P. Ilten et al., *An introduction to PYTHIA 8.2*, *Comput. Phys. Commun.* **191** (2015) 159 [[1410.3012](#)].
- [77] DELPHES 3 collaboration, *DELPHES 3, A modular framework for fast simulation of a generic collider experiment*, *JHEP* **02** (2014) 057 [[1307.6346](#)].
- [78] Y.-C. Guo, F. Feng, A. Di, S.-Q. Lu and J.-C. Yang, *MAnalysis: An open-source program for high energy physics analyses*, *Comput. Phys. Commun.* **294** (2024) 108957 [[2305.00964](#)].
- [79] ATLAS collaboration, *Studies of $Z\gamma$ production in association with a high-mass dijet system in pp collisions at $\sqrt{s} = 8$ TeV with the ATLAS detector*, *JHEP* **07** (2017) 107 [[1705.01966](#)].
- [80] G. Cowan, K. Cranmer, E. Gross and O. Vitells, *Asymptotic formulae for likelihood-based tests of new physics*, *Eur. Phys. J. C* **71** (2011) 1554 [[1007.1727](#)].
- [81] PARTICLE DATA GROUP collaboration, *Review of Particle Physics*, *PTEP* **2020** (2020) 083C01.